united nations
educational, scientific
and cultural
organization

international atomic
energy agency

the
abdus salam
international centre for theoretical physics

SMR 1161/26

AUTUMN COLLEGE ON PLASMA PHYSICS

25 October - 19 November 1999

Introduction to Particle-in-Cell Techniques

J.P. VERBONCOEUR

University of California,
Dept. of Electrical Engineering and Computer Science
Berkeley, U.S.A.

Introduction to Particle-in-Cell Techniques

J. P. Verboncoeur
Plasma Theory and Simulation Group
Department of Electrical Engineering and Computer Science
University of California
Berkeley, CA 94720-1770
http://ptsg.eecs.berkeley.edu

1999 ICTP
Grignano, Italy

Nov. 8-11, 1999

Contents

1 PIC Overview

The Particle-in-Cell technique grew out of electron trajectory simulation in the 1950s, lead by O. Buneman [4] and J. M. Dawson [6]. The self-consistent PIC method was formalized and codified in the 1960s-1980s by C. K. Birdsall and A. B. Langdon [2], and R. W. Hockney and J. W. Eastwood [12].

The PIC model has been used to simulate a wide variety of applications:

- basic plasma physics: waves and instabilities
- magnetic fusion
- gaseous discharges (pressures ranging from mTorr to 720 Torr)
- electron and ion optics
- microwave-beam devices
- plasma-filled microwave-beam devices

Range of validity:

- low pressure discharges (or $pd < 0.1$ m-Torr)
- kinetic
- nonlinear
- time-dependent
- self-consistent
- fully relativistic
- electrostatic or electromagnetic
- often can include full macroscopic physics models - few approximations

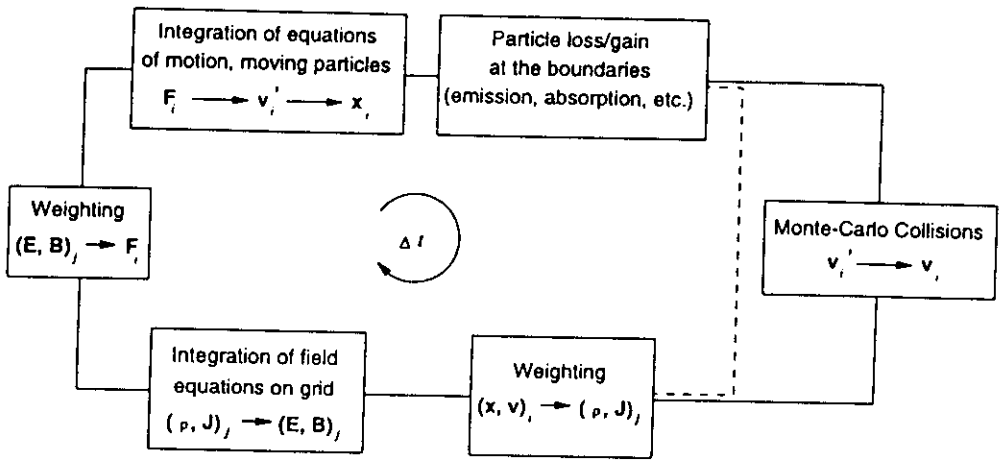

Figure 1: Flow chart for an explicit PIC-MCC scheme.

2 PIC-MCC Flow Chart

The PIC scheme is shown schematically in Fig. 1. Particle and field values are advanced sequentially in time, starting from initial conditions. The particle equations of motion are advanced one time step, using fields interpolated from the discrete grid to the continuous particle locations. Next, particle boundary conditions such as absorption and emission are applied. If the model is collisional, the Monte Carlo collision (MCC) scheme is applied (see below for details). Source terms, ρ and J, for the field equations are accumulated from the continuous particle locations to the discrete mesh locations. The fields are then advanced one timestep, and the timestep loop starts over again.

3 Particle Equations of Motion

The Newton-Lorentz equations of motion can be written:

$$\frac{d}{dt}\gamma m\mathbf{v} = \mathbf{F} = q\left(\mathbf{E} + \mathbf{v} \times \mathbf{B}\right) \text{ and} \tag{1}$$

$$\frac{d}{dt}\mathbf{x} = \mathbf{v}, \tag{2}$$

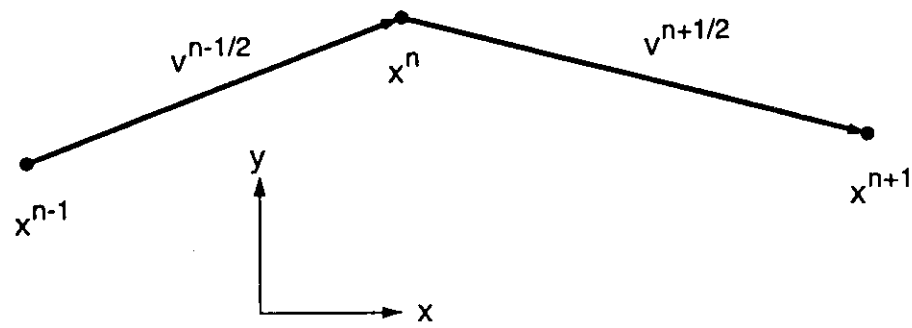

Figure 2: Schematic leapfrog integration.

where

$$\gamma = \sqrt{\frac{1}{1-(v/c)^2}} = \sqrt{1+(u/c)^2}, \tag{3}$$

$$u = \gamma v. \tag{4}$$

Often integrated using the *leapfrog* integrator:

- Second order accurate
- Requires few operations
- Requires minimal storage
- Stable for $\omega_p \Delta t < 2$

In finite difference form the leapfrog method yields:

$$\frac{\mathbf{u}^{t+\Delta t/2} - \mathbf{u}^{t-\Delta t/2}}{\Delta t} = \frac{q}{m}\left(\mathbf{E}^t + \frac{\mathbf{u}^{t+\Delta t/2} + \mathbf{u}^{t-\Delta t/2}}{2\gamma^t} \times \mathbf{B}^t\right) \tag{5}$$

$$\frac{\mathbf{x}^{t+\Delta t} - \mathbf{x}^t}{\Delta t} = \frac{\mathbf{u}^{t+\Delta t/2}}{\gamma^{t+\Delta t/2}} \tag{6}$$

An efficient technique for integration of Eq. 5 is due to Boris [3]:

$$\mathbf{u}^- = \mathbf{u}^{t-\Delta t/2} + \frac{q\Delta t \mathbf{E}^t}{2m} \tag{7}$$

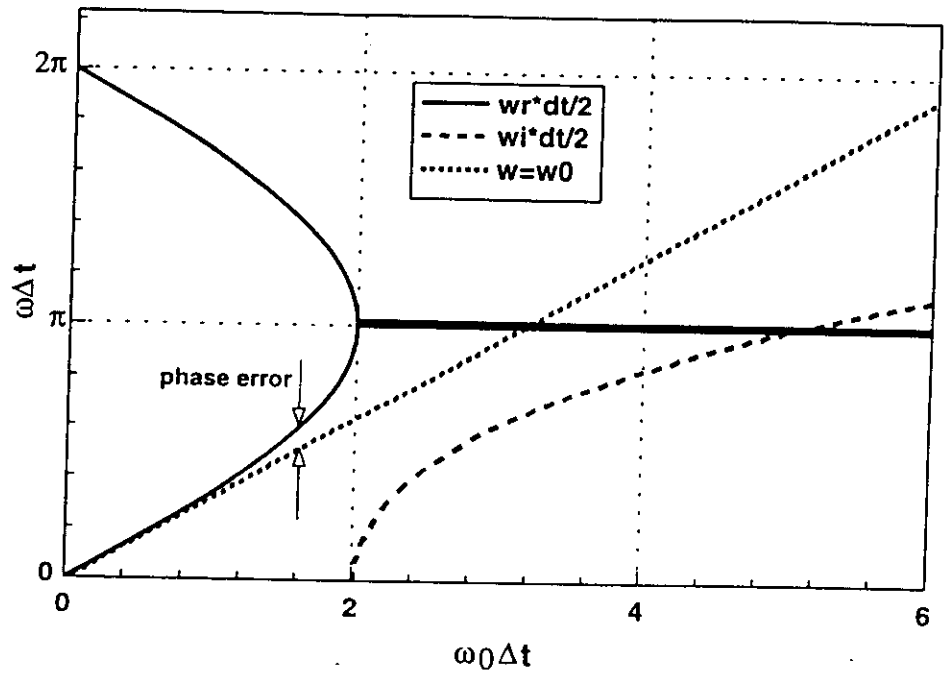

Figure 3: Leapfrog solution for simple harmonic motion.

$$\mathbf{u}' = \mathbf{u}^- + \mathbf{u}^- \times \mathbf{t}^t \tag{8}$$

$$\mathbf{u}^+ = \mathbf{u}^- + \mathbf{u}' \times \frac{2\mathbf{t}^t}{1 + \mathbf{t}^t \cdot \mathbf{t}^t} \tag{9}$$

$$\mathbf{u}^{t+\Delta t/2} = \mathbf{u}^+ + \frac{q\Delta t \mathbf{E}^t}{2m}, \tag{10}$$

with

$$\mathbf{t}^t = \hat{\mathbf{B}} \tan\left(\frac{q\Delta t}{2\gamma^t m} B^t\right). \tag{11}$$

Note that Eqs. 8-9 represent a rotation only, i.e. $\mathbf{u}^- \cdot \mathbf{u}^- = \mathbf{u}^+ \cdot \mathbf{u}^+$.

Stability of the leapfrog mover can be demonstrated for simple harmonic motion. Consider the simple harmonic oscillator

$$\frac{d^2x}{dt^2} = -\omega_0^2 x \tag{12}$$

Finite difference using a center difference (leapfrog):

$$\frac{x^{t+\Delta t} - 2x^t + x^{t-\Delta t}}{\Delta t^2} = -\omega_0^2 x^t \tag{13}$$

Solutions are of the form

$$x^t = C \exp\left(-i\omega t\right), \tag{14}$$

$$x^{t+\Delta t} = C \exp\left(-i\omega \left(t + \Delta t\right)\right). \tag{15}$$

Using Euler's Eq., the finite difference becomes

$$\sin\left(\frac{\omega \Delta t}{2}\right) = \pm \frac{\omega_0 \Delta t}{2}, \tag{16}$$

so ω has an imaginary component for $\omega_0 \Delta t > 2$, indicating numerical instability. Expanding Eq. 16 for $\omega \Delta t \ll 1$:

$$\frac{\omega \Delta t}{2}\left[1 - \frac{1}{6}\left(\frac{\omega \Delta t}{2}\right)^2 + O\left(\frac{\omega \Delta t}{2}\right)^4\right] = \frac{\omega_0 \Delta t}{2}, \tag{17}$$

we find the phase error is quadratic.

3.1 Cylindrical Coordinates

For cylindrical coordinates, the anguiar momentum must be considered. Boris [3] proposed a solution involving a transform to Cartesian coordinates, followed by a rotation of the coordinate system, and translation back to the cylindrical coordinate system. Note that the advance in z is identical to the Cartesian advance.

For a particle with position $\mathbf{x}^t$, velocity $\mathbf{v}^{t+\Delta t/2}$, the coordinate system $\left(x', y'\right)$ is created such that $\hat{x}' = \hat{r}$ and $\hat{y}' = \hat{\theta}$ for $\mathbf{x}^t$. Then

$$x_1' = r_1 \tag{18}$$

$$y_1' = 0 \tag{19}$$

Next, the particle is advanced in the $\left(x', y'\right)$ system:

$$x_2' = r_1 + v_{r1} \Delta t \tag{20}$$

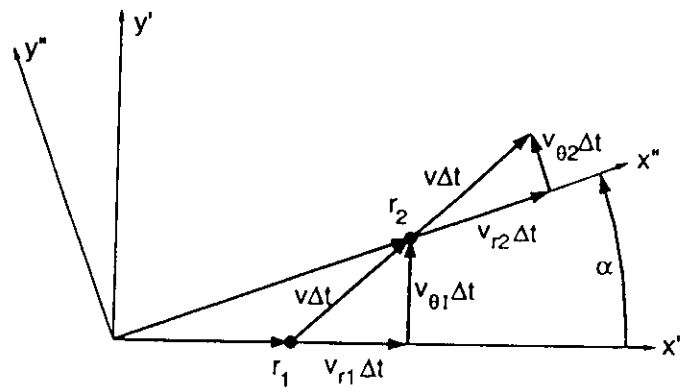

Figure 4: Rotated coordinate system for cyclindrical position advance and velocity vector rotation.

$$y_2^{'} = v_{\theta 1} \Delta t. \tag{21}$$

Converting to cylindrical coordinates in the $(x^{''}, y^{''})$ system:

$$r_2 = \sqrt{\left(x_2^{'}\right)^2 + \left(y_2^{'}\right)^2} \tag{22}$$

$$\theta_2 = \theta_1 + \alpha \tag{23}$$

Converting the velocity using a rotation into the new coordinate system:

$$v_{r2} = v_{r1} \cos\alpha + v_{\theta 1} \sin\alpha \tag{24}$$

$$v_{\theta 2} = -v_{r1} \sin\alpha + v_{\theta 1} \cos\alpha \tag{25}$$

$$\sin\alpha = \frac{y_2^{'}}{r_2} \tag{26}$$

$$\cos\alpha = \frac{x_2^{'}}{r_2} \tag{27}$$

When $r_2 \rightarrow 0$, let $\cos\alpha = 1$, $\sin\alpha = 0$ (all momentum radial).

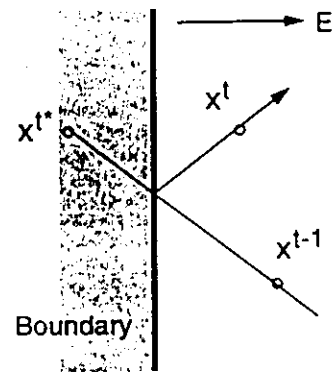

Figure 5: Reflection at a boundary.

3.2 Particle Boundary and Initial Conditions

3.2.1 Absorption

- Conductor: absorb charge, add to the global σ (floating vs. circuit)
- Dielectric: deposit charge, weight q locally to mesh
- bookkeeping: repack particle arrays
- noise – hard vs. soft (gradual absorption) bc [14]

3.2.2 Reflection

- Physical Reflection: reverse $x_{bc} - x \rightarrow x_{bc} + x$, $-v_x \rightarrow v_x$
- Symmetry Boundary: also reverse v_y and v_z to preserve sense of magnetization
- Specular Reflection – 1st order error [14]

$$v^{t-\Delta t/2*} = -v^{t-\Delta t/2} + \frac{qE}{m}\left(\frac{2\left|x^t - x_{bc}\right|}{\left|v^{t-\Delta t/2}\right|} - \Delta t\right) \tag{28}$$

Note that average error is zero, but there is net heating due to the phase space diffusion:

$$\Delta v_{rms} = \frac{qE}{m}\frac{\Delta t}{\sqrt{3}} \tag{29}$$

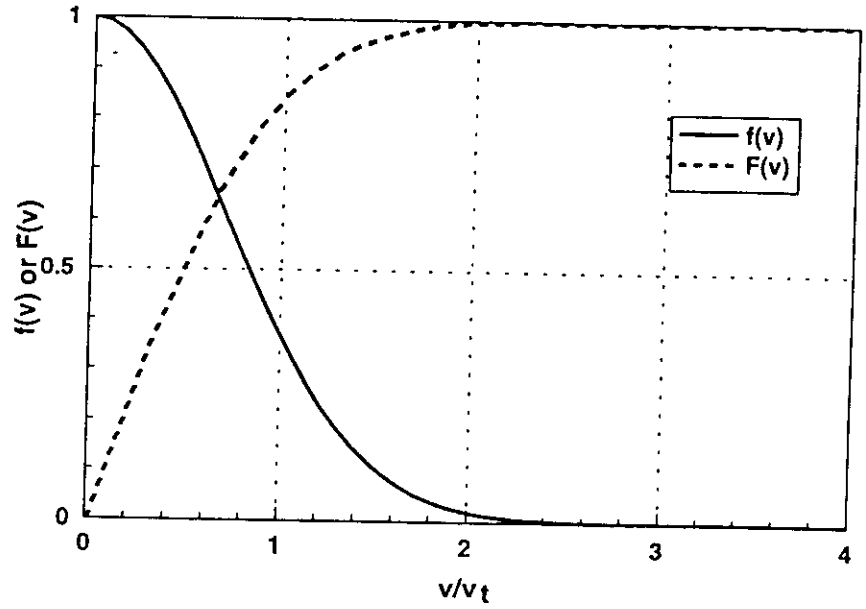

Figure 6: Distribution function, $f(v)$, and cumulative distribution function, $F(v)$, for a Maxwell-Boltzmann distribution.

3.2.3 Loading Initial Distributions

Maxwell-Boltzmann distribution:

$$f(\mathcal{E}) = f_0 \exp\left(-\frac{\mathcal{E}}{kT}\right) \tag{30}$$

$$\mathcal{E} = \frac{1}{2}mv_t^2 = \frac{3}{2}kT \tag{31}$$

In one dimension:

$$f(v_i) = f_{0i} \exp\left(-\frac{v_i^2}{v_{ti}^2}\right) \tag{32}$$

$$\frac{1}{2}mv_{ti}^2 = \frac{1}{2}kT \tag{33}$$

Invert the cumulative distribution function,

$$F(v_i) = \frac{\int_0^{v_i} \exp\left(-v^2/v_t^2\right) dv}{\int_0^{\infty} \exp\left(-v^2/v_t^2\right) dv} \tag{34}$$

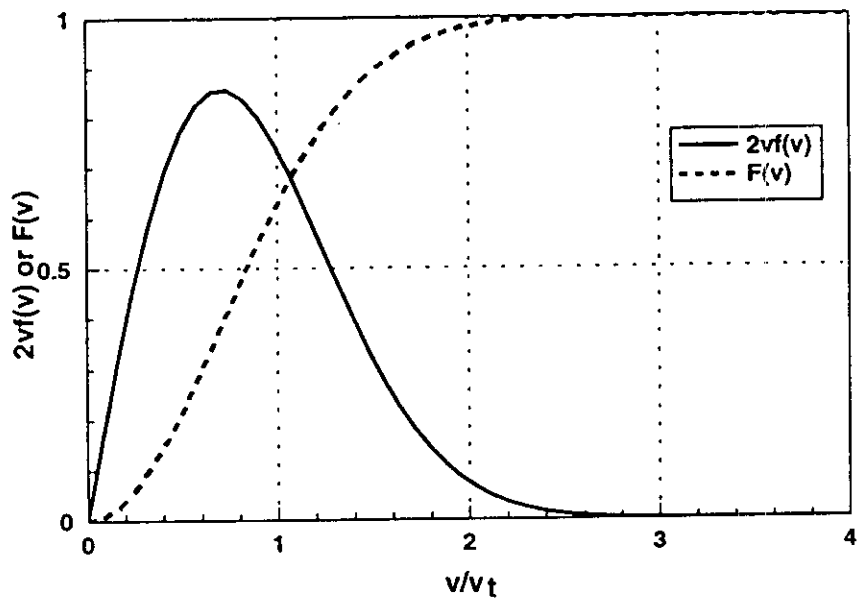

Figure 7: Flux distribution function, $vf(v)$, and cumulative flux distribution function, $F(v)$, for a Maxwell-Boltzmann distribution.

Box-Muller method [21]: choose 2 pseudo-random numbers, $0 < \nu_1, \nu_2 \leq 1$. Discard if $R^2 = \nu_1^2 + \nu_2^2 > 1$. Then

$$v_1 = \nu_1 \sqrt{-\frac{\ln(R^2)}{R^2}}, \tag{35}$$

$$v_2 = \nu_2 \sqrt{-\frac{\ln(R^2)}{R^2}} \tag{36}$$

Eq. 34 must be inverted numerically for general cutoffs.

3.2.4 Injection

Cumulative distribution for thermal flux:

$$F(v_i) = \frac{\int_{v_{cl}}^{v_i} v \exp(-v^2/v_t^2)\, dv}{\int_{v_{cl}}^{v_{cu}} v \exp(-v^2/v_t^2)\, dv} = \mathcal{R} \tag{37}$$

$$v_i = \sqrt{v_{cl}^2 + v_{cu}^2 - v_t^2 \ln\left(\mathcal{R} \exp(v_{cl}^2/v_t^2) + (1-\mathcal{R}) \exp(v_{cu}^2/v_t^2)\right)} \tag{38}$$

without cutoffs,

$$v_i = v_t\sqrt{-\ln(\mathcal{R})} \tag{39}$$

For drifting Maxwellian:

$$F(v_i) = \frac{\int_{v_{cl}}^{v_i} v\exp\left(-\left(v-v_0\right)^2/v_t^2\right)dv}{\int_{v_{cl}}^{v_{cu}} v\exp\left(-\left(v-v_0\right)^2/v_t^2\right)dv} = \mathcal{R} \tag{40}$$

$$= \frac{e^{(v_{cl}-v_0)^2/v_t^2} - e^{(v_i-v_0)^2/v_t^2} + \sqrt{\pi}\frac{v_0}{v_t}\left(\mathrm{Erf}\left(\left(v_i-v_0\right)/v_t\right) - \mathrm{Erf}\left(\left(v_{cl}-v_0\right)/v_t\right)\right)}{e^{(v_{cl}-v_0)^2/v_t^2} - e^{(v_{cu}-v_0)^2/v_t^2} + \sqrt{\pi}\frac{v_0}{v_t}\left(\mathrm{Erf}\left(\left(v_{cu}-v_0\right)/v_t\right) - \mathrm{Erf}\left(\left(v_{cl}-v_0\right)/v_t\right)\right)} \tag{41}$$

which must be inverted numerically.

3.2.5 Photoemission

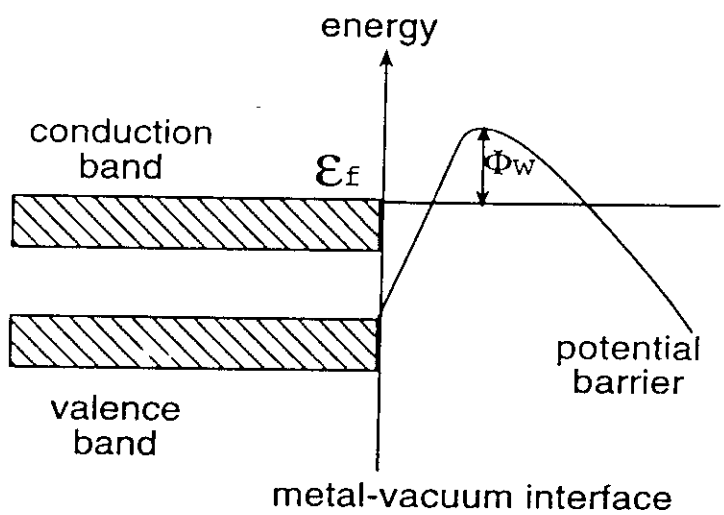

Figure 8: Potential energy schematic at a metal surface.

- Work function: $\Phi_w = \Phi(E=0) - \mathcal{E}_F \approx 2-5$ eV.
- Irradiation energy $\hbar\omega \geq \Phi_w$
- Ejected electron carries away additional energy $\mathcal{E} = \hbar\omega - \Phi_w$

3.2.6 Thermionic Emission

- Electrons are heated to $\mathcal{E} > \mathcal{E}_F + \Phi_w$
- Current given by Richardson-Dushman Equation [7]:

$$J = 120T^2 \exp\left(-e\Phi_w/kT\right) \text{ A/cm}^2 \tag{42}$$

- T = absolute temperature of cathode.
- Typical current densities $J \lesssim 100$ A/cm^2.

3.2.7 Fowler-Nordheim Field Emission

- Fowler Nordheim Law [9]:

$$J_{FN} = \frac{AE^2}{\Phi_w t^2(y)} \exp\left(\frac{-Bv(y)\Phi_w^{3/2}}{E}\right) \text{ A/m}^2 \tag{43}$$

- E = normal component of electric field at surface
- $B = 6.8308\times10^9$
- $A = 1.5414\times10^{-6}$
- $t^2(y) \approx 1.1$
- $v(y) = 0.95 - y^2$
- $y = 3.79 \times 10^{-5} E^{1/2}/\Phi_w$

3.2.8 Child's Law Field Emission

- Current given by Child's Law over first cell:

$$J_{CL} = \frac{4\varepsilon_0}{9}\sqrt{2\frac{e}{m}}\frac{\left(-E_{1/2}\Delta x\right)^{3/2}}{\Delta x^2} \tag{44}$$

- $E_{1/2}$ = normal field at the first half cell
- Δx = width of the first cell normal to the surface
- $J_{CL} \to 0$ when the field reverses
- Does not allow self-consistent formation of virtual cathode

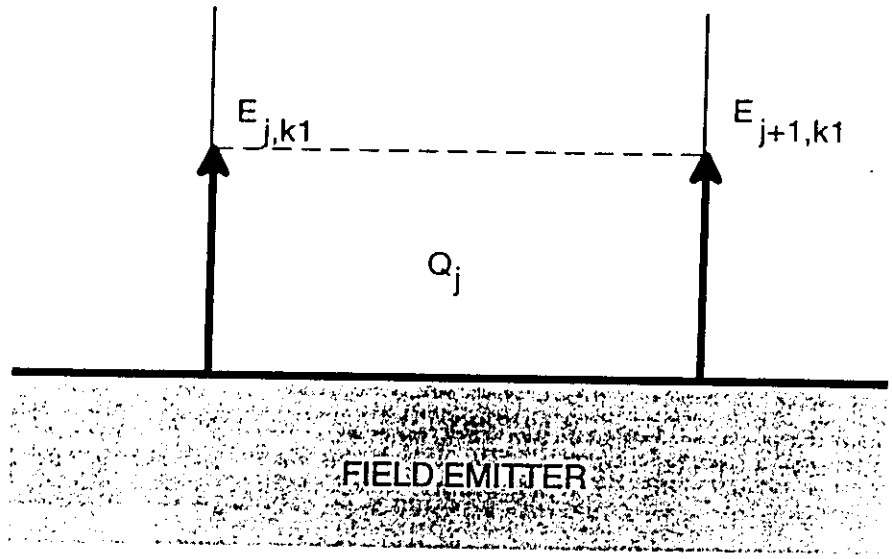

Figure 9: Schematic of 1st cell near Gauss's law field emitter.

3.2.9 Gauss's Law Field Emission

- Attempts to inject space charge sufficient to obtain $E \rightarrow 0$ at the emitter surface

$$Q_j = \int_{cell} \mathrm{D} \cdot d\mathrm{S} = \varepsilon_{j+1/2,k1} d\mathrm{S}_{j+1/2,k1} \frac{(E_{j,k1} + E_{j+1,k1})}{2} \qquad (45)$$

- Q_j = the space charge to inject in the cell
- $d\mathrm{S}_{j+1/2}$ = surface area normal to the cell
- initial position chosen just inside surface (many authors place randomly in the first half cell)

3.2.10 Secondary Emission

The process of electron impact secondary emission is a key element of a number of processes related to high power microwave tubes. Secondary emission plays a pivotal role in depressed collectors, single- and two-surface multipactors, and beam interception. In this section, a secondary emission model

is outlined, and the implementation in the XOOPIC PIC-MCC code [34] is described.

Electron impact secondary emission occurs when an electron impacts a surface, which may be a conductor or a dielectric, and ejects electrons from the surface. In PIC codes, it is not possible to model the quantum mechanical details of the process, which involves interaction of the incident electron with conduction or valence band electrons in the surface medium, due to the time and space scales involved. Instead, it is more efficient to employ a phenomenological model.

This work is based on the secondary model due to Vaughan [31] and later experimentally verified by Shih [26], and improved by Vaughan [32] and later [10]. The secondary electron coefficient, defined as the ratio of ejected to incident electrons, has both energy and angular dependence:

$$\delta\left(\mathcal{E},\theta\right) = \delta_{\mathrm{max0}}\left(1 + k_{s\delta}\frac{\theta^2}{2\pi}\right)\left(w\exp\left(1-w\right)\right)^k. \tag{46}$$

Here, the incident energy is given by $\mathcal{E}$, the angle with respect to the surface normal is θ, $k_{s\delta}$ is a surface smoothness parameter described below, k is a curve-fit parameter also described below, and δ_{max0} is the peak coefficient, which occurs at normal incidence at the energy $\mathcal{E}_{\mathrm{max0}}$. The energy dependence appears implicitly in the right hand side of Eq. 46 through the normalized energy, w, given by:

$$w = \frac{\mathcal{E}-\mathcal{E}_0}{\mathcal{E}_{\mathrm{max0}}\left(1+k_{sw}\theta^2/2\pi\right)-\mathcal{E}_0}, \tag{47}$$

where $\mathcal{E}_0$ is the secondary emission threshold and k_{sw} is a surface-smoothness parameter similar to $k_{s\delta}$. Both $k_{s\delta}$ and k_{sw} vary between 0 for very rough surfaces and 2 for polished surfaces. Typical values are close to 1. The exponent k in Eq. 46 is given by:

$$k = \begin{cases} 0.62, & w < 1 \\ 0.25, & w \geq 1 \end{cases}. \tag{48}$$

The energy dependence of the secondary emission coefficient is shown in Fig. 10. The angular dependence of the secondary emission coefficient is shown in Fig. 11. Note that the secondary emission coefficient, which can be obtained by multiplying the energy dependent part by the angular dependent

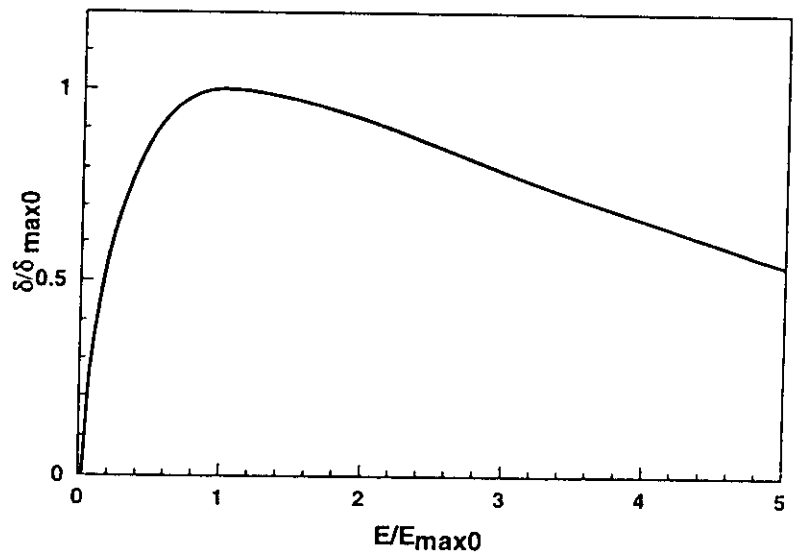

Figure 10: Normalized secondary emission coefficient as function of normalized energy at normal incidence, with $\mathcal{E}_{\max 0}/\mathcal{E}_0 = 40$, and $k_{sw} = 1$.

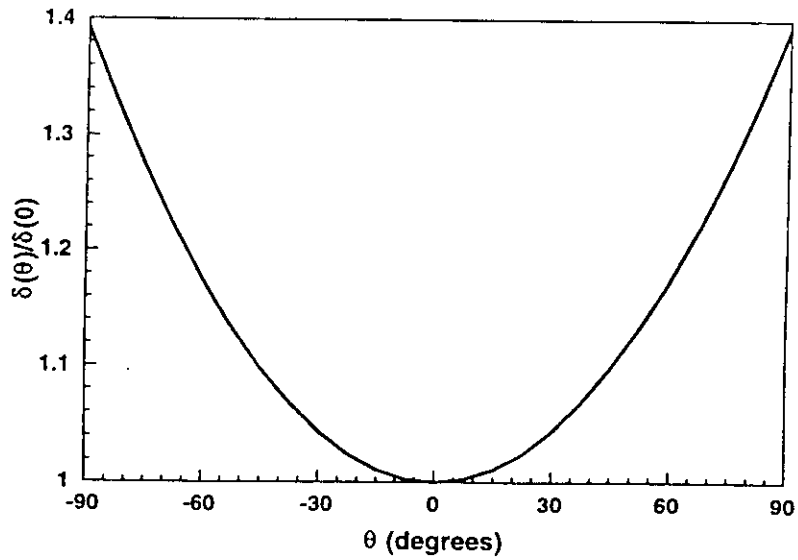

Figure 11: Angular dependence of the secondary emission coefficient normalized to the coefficient at normal incidence to the surface. Here $k_{s\delta} = 0$.

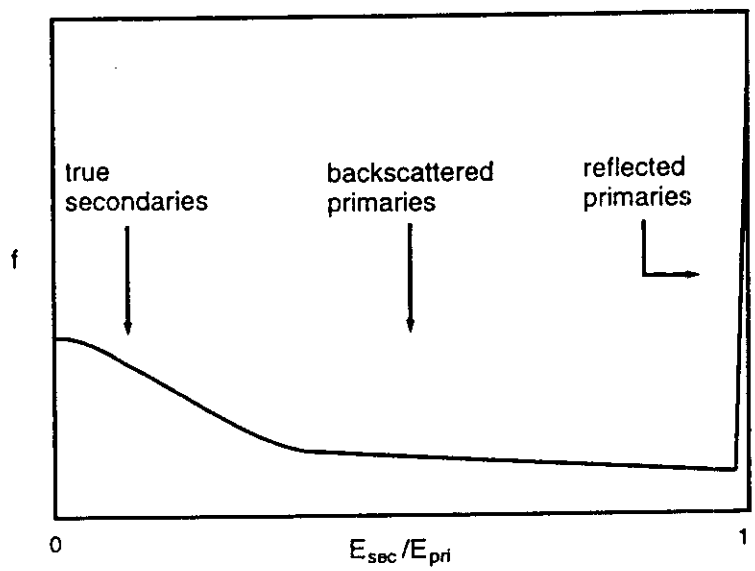

Figure 12: Schematic diagram of the secondary emission spectrum versus the ratio of the emitted energy of the secondary to the incident energy of the primary.

part, is largest at $\mathcal{E} = \mathcal{E}_{max\,0}$ and $\theta = 90$. The peak normal secondary emission in copper is $\delta_{max\,0} = 1.2$, with $\mathcal{E}_{max\,0} = 400$ eV, and $\mathcal{E}_0 = 15$.

The energy and angular distribution of the emitted secondaries were treated by Spangenberg [27], and are also treated by Vaughan [31]. The emission spectrum has three regimes, as shown in Fig. 12. Incident electrons reflected at the surface of the secondary emitting material are called reflected primaries. Reflected primaries comprise about 3% of the emitted electron population. The energy of the reflected primary is approximately the same as the energy of the incident primary, $\mathcal{E}_r = \mathcal{E}_i$. The primary is reflected specularly in angle, $\theta_r = -\theta_i$, where θ is measured from the surface normal at the point of impact.

Backscattered primaries are electrons that impact the surface, and scatter off of several lattice atoms and/or impurities. Typically backscattered primaries comprise about 7% of the emitted electron population. These electrons re-emerge from the impact surface with energies in the range $0 < \mathcal{E}_b < \mathcal{E}$. Within this energy range, all energies are taken as equally probable, $\mathcal{E}_b = R\mathcal{E}_i$, where $0 \leq R < 1$ is a uniformly distributed random number. The

angle of emission is taken to be specular, just as in the case of the reflected primaries. A more detailed treatment might consider a distribution of angles resulting from quantum mechanical treatment of scattering in the lattice potentials in the secondary emission medium.

True secondaries are electrons that are emitted from the conduction or valence bands of the atoms comprising the impact surface. The emitted electron population contains about 90% true secondaries. Energy is imparted to the lattice electrons over some time long compared to the elastic collision time, so the electron energy distribution can be modeled as a Maxwell-Boltzmann distribution. The electrons are emitted with energies from a thermal distribution of temperature T:

$$f(\mathcal{E}) = \frac{\mathcal{E}}{(k_B T)^2} \exp\left(\frac{-\mathcal{E}}{k_B T}\right), \tag{49}$$

where k_B is Boltzmann's constant. Due to the timescale of the emission process, the angle of emission can be taken to be isotropic:

$$g(\theta) = \frac{\cos(\theta)}{2}. \tag{50}$$

The secondary model described above has been implemented in part in the XPDP1 code [33], and in full in the XOOPIC code [34]. In the scheme described above, the secondary emission coefficient can indicate that a fractional number of electrons must be emitted. The above codes emit fractional electron yields statistically, using a random number. Another technique is to accumulate fractional particles until a sufficient level is achieved to emit a particle. Variable particle weighting can also be used to represent fractional electron emission [23]. The secondary electrons are typically computed after each electron is absorbed at a surface, at the end of a timestep, and advanced into the simulation in the next timestep (XPDP1). Riyopoulus [24] has noted a banding effect when emitting at the end of a timestep, due to an average emission delay of $\Delta t/2$. This was repaired by computing a fractional step for emission which accounts for the time within the timestep that the particle impacted the emission surface. XOOPIC is capable of advancing each particle the remaining fraction of the timestep, eliminating this problem. The banding effect is observed only for large timesteps, $\omega_{rf}\Delta t/2 \approx 1$, where ω_{rf} is the driving frequency of the multipactor in the Riyopoulus study.

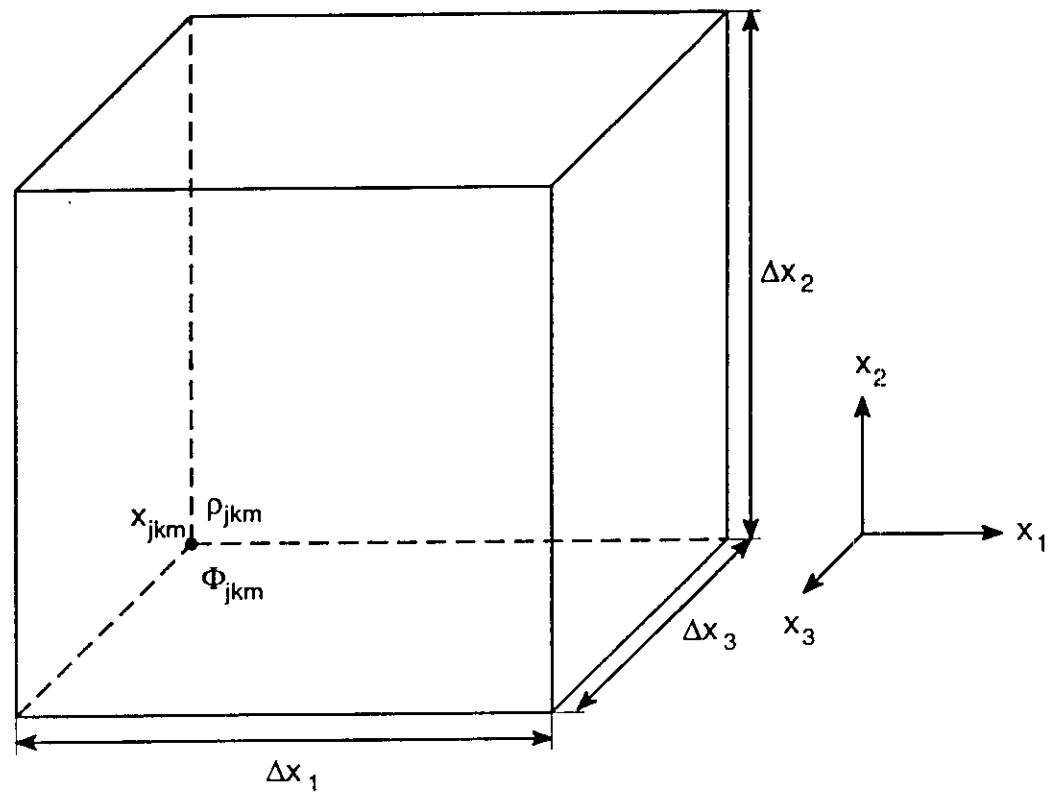

Figure 13: Charge density and electrostatic potential on a grid. Electric fields, not shown, are co-located with the potentials.

4 Electrostatic Field Model

Assume we have a gridded system with charge density $\rho_{j,k}$ known at the nodes. We wish to obtain the potentials and fields at the nodes using Poisson's equation (from Gauss's law, $\nabla \cdot \varepsilon \mathbf{E} = \rho$, and $\mathbf{E} = -\nabla\Phi$):

$$\nabla \cdot \varepsilon \nabla \Phi(\mathbf{x}, t) = \rho(\mathbf{x}, t) \tag{51}$$

This can be solved in finite difference form in a number of ways. Using a center difference in a 1d linear homogeneous isotropic medium, we obtain

$$\frac{\Phi_{j+1} - 2\Phi_j + \Phi_{j-1}}{\Delta x^2} = -\frac{\rho_j}{\varepsilon}. \tag{52}$$

Physically, the boundary conditions can be complicated [33]. For a fully bounded system, the charge is conserved:

$$\oint_S \epsilon \mathbf{E} \cdot d\mathbf{S} = \int_V \rho dV + \oint_S (\sigma_0 + \sigma_J) dS \equiv 0 \tag{53}$$

In general, the electric field is assumed to be zero beyond the electrodes, so that just inside the system (Gauss's law),

$$E_0 = \frac{\sigma_0}{\epsilon} \tag{54}$$

$$E_J = -\frac{\sigma_J}{\epsilon} \tag{55}$$

Mathematically, a Dirichlet boundary condition is required for a unique solution; often one chooses a reference potential of zero at one of the electrodes (e.g. $\Phi_J = 0$).

For a non-uniform orthogonal Cartesian mesh in two dimensions, Eq. 51 can be center differenced:

$$\begin{aligned} &\frac{\Phi_{j,k+1}}{\Delta x_{k+1/2}\Delta \bar{x}_k} - \frac{2\Phi_{j,k}}{\Delta x_{k+1/2}\Delta x_{k-1/2}} + \frac{\Phi_{j,k-1}}{\Delta x_{k-1/2}\Delta \bar{x}_k} + \\ &\frac{\Phi_{j+1,k}}{\Delta y_{j+1/2}\Delta \bar{y}_j} - \frac{2\Phi_{j,k}}{\Delta y_{j+1/2}\Delta x_{j-1/2}} + \frac{\Phi_{j-1,k}}{\Delta y_{j-1/2}\Delta \bar{y}_j} \\ = \; & -\frac{\rho_{j,k}}{\epsilon}, \end{aligned} \tag{56}$$

with

$$\Delta x_{k+1/2} = x_{k+1} - x_k \tag{57}$$

$$\Delta \bar{x}_k = \frac{\Delta x_{k+1/2} + \Delta x_{k-1/2}}{2} \tag{58}$$

and likewise for other subscripts and components. A Taylor expansion gives the truncation error:

$$\begin{aligned} \nabla^2\Phi - \nabla^2\Phi_{exact} = \; & \frac{\Delta x_{k+1/2} - \Delta x_{k-1/2}}{3}\Phi_{xxx} + \frac{\Delta y_{j+1/2} - \Delta y_{j-1/2}}{3}\Phi_{yyy} \\ & + \frac{(\Delta x_{k+1/2})^2 - \Delta x_{k+1/2}\Delta x_{k-1/2} + (\Delta x_{k-1/2})^2}{12}\Phi_{xxxx} \\ & + \frac{(\Delta y_{j+1/2})^2 - \Delta y_{j+1/2}\Delta y_{j-1/2} + (\Delta y_{j-1/2})^2}{12}\Phi_{yyyy} + \ldots \end{aligned} \tag{59}$$

which contains first order terms for $\Delta x_{k+1/2} \neq \Delta x_{k-1/2}$. On a uniform mesh, only the second order error terms remain.

The potential can be separated into a Poisson and Laplace parts [29]:

$$\Phi = \Phi_P + \sum_{boundaries} \Phi_L \tag{60}$$

$$\nabla \cdot \varepsilon \nabla \Phi_P = -\rho \tag{61}$$

$$\nabla \cdot \varepsilon \nabla \Phi_{Li} = 0 \tag{62}$$

The boundary conditions for Eq. 61 become $\Phi = 0$ on all boundaries. For each boundary with a Dirichlet condition, Eq. 62 is solved for $\Phi_i = 1$ on the equipotential surface, and $\Phi = 0$ elsewhere. The resulting Φ_{Li} can be stored and multiplied by a constant if the potential on the boundary is specified as a function of time or the result of an external circuit equation. Neumann boundary conditions are included through Φ_P. This method neglects charge induced by a driven electrode on other boundaries which are connected to an external circuit. This problem is avoided, at the expense of increased matrix size, when solving the full Poisson equation with boundaries and circuits using the method of Verboncoeur [33].

4.1 Electrostatic Boundary Conditions: External Circuit

The boundary conditions for the field equations in one dimension can be considered as a circuit. See [33] for additional details.

- Short Circuit (ideal voltage source): $\Phi_0(t)$ is specified, $\Phi_J = 0$
- Open Circuit (floating electrode): from Gauss's Law,

$$E_{1/2} = \frac{\Phi_0^t - \Phi_1^t}{\Delta x} = \frac{\sigma_0^t + \rho_0^t \Delta x/2}{\varepsilon} \tag{63}$$

$$\sigma_0^t = \sigma_0^{t-\Delta t} - \int_{t-\Delta t}^{t} J_{plasma} dt \tag{64}$$

- Voltage Driven Series RLC Circuit: Voltage drop around an RLC can be written using the Kirchhoff voltage law:

$$L\frac{d^2Q(t)}{dt^2} + R\frac{dQ(t)}{dt} + \frac{Q(t)}{C} = V(t) + \Phi_J(t) - \Phi_0(t). \tag{65}$$

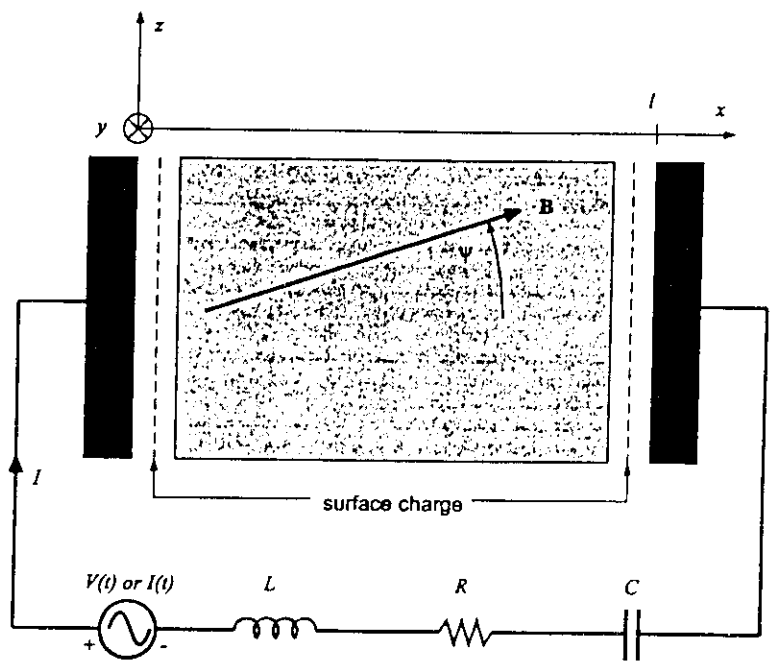

Figure 14: Schematic one-dimensional bounded plasma with external circuit.

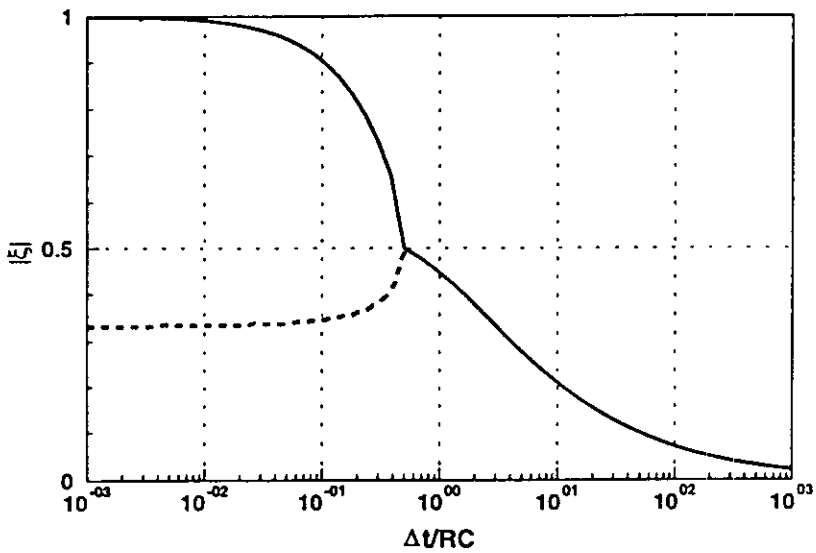

Figure 15: Roots of the characteristic equation in the limit $L \to 0$. The scheme can only follow the RC time when $\Delta t < RC/2$.

One second order difference is

$$Q^t = \frac{V(t) + \Phi_J^t - \Phi_0^t - K^t}{\alpha_0}, \tag{66}$$

where

$$K^t = \alpha_1 Q^{t-\Delta t} + \alpha_2 Q^{t-2\Delta t} + \alpha_3 Q^{t-3\Delta t} + \alpha_4 Q^{t-4\Delta t}, \tag{67}$$

$$\alpha_0 = \frac{9}{4}\frac{L}{\Delta t^2} + \frac{3}{2}\frac{R}{\Delta t} + \frac{1}{C}, \tag{68}$$

$$\alpha_1 = -6\frac{L}{\Delta t^2} - 2\frac{R}{\Delta t}, \tag{69}$$

$$\alpha_2 = \frac{11}{2}\frac{L}{\Delta t^2} + \frac{1}{2}\frac{R}{\Delta t}, \tag{70}$$

$$\alpha_3 = -2\frac{L}{\Delta t^2}, \tag{71}$$

$$\alpha_4 = \frac{1}{4}\frac{L}{\Delta t^2}. \tag{72}$$

The circuit is coupled to the Poisson equation using conservation of charge at an electrode:

$$\sigma_0^t = \sigma_0^{t-\Delta t} - \int_{t-\Delta t}^{t} J_{plasma} dt + \frac{Q^t - Q^{t-\Delta t}}{A} \tag{73}$$

Stability of the circuit with $L \to 0$ is given by the characteristic equation:

$$\xi^2 \left(3 + \frac{2\Delta t}{RC}\right) - 4\xi + 1 = 0 \tag{74}$$

The characteristic equation for the full RLC circuit is given by

$$\xi^4 \left(9 + 6\tau_1 + 4\tau_2^2\right) - \xi^3 \left(24 + 8\tau_1\right) + \xi^2 \left(22 + 2\tau_1\right) - 8\xi + 1 = 0, \tag{75}$$

$$\tau_1 = \frac{R\Delta t}{L} \tag{76}$$

$$\tau_2 = \frac{\Delta t}{\sqrt{LC}} \tag{77}$$

5 Electromagnetic Field Model

The solution to Maxwell's equations typically involves solving finite-difference time-domain (FDTD) discretizations on a Yee mesh, with the fields defined as shown in Fig. 16. In addition, the electric field is known at integral multiples of the timestep, while the magnetic field is known at $t = (n + 1/2)\,\Delta t$, where n is an integer. Even for an electromagnetic simulation, the initial conditions may require solution of the Poisson equation, $\nabla \cdot \varepsilon \nabla \Phi = -\rho$. In addition, initial magnetic fields due to external magnets and coils may be prescribed analytically or in tabular format, and must satisfy $\nabla \cdot \mathbf{B} = 0$.

Once the initial conditions are computed, the electric and magnetic fields are then advanced in time using finite-differenced forms of Faraday's law and Ampere's law. The remaining Maxwell equations, $\nabla \cdot \mathbf{B} = 0$ and $\nabla \cdot \mathbf{D} = \rho$ remain satisfied in time when satisfied by the initial conditions.

Starting with Ampere's law,

$$\frac{\partial \mathbf{D}}{\partial t} = \nabla \times \mathbf{H} - \mathbf{J}, \tag{78}$$

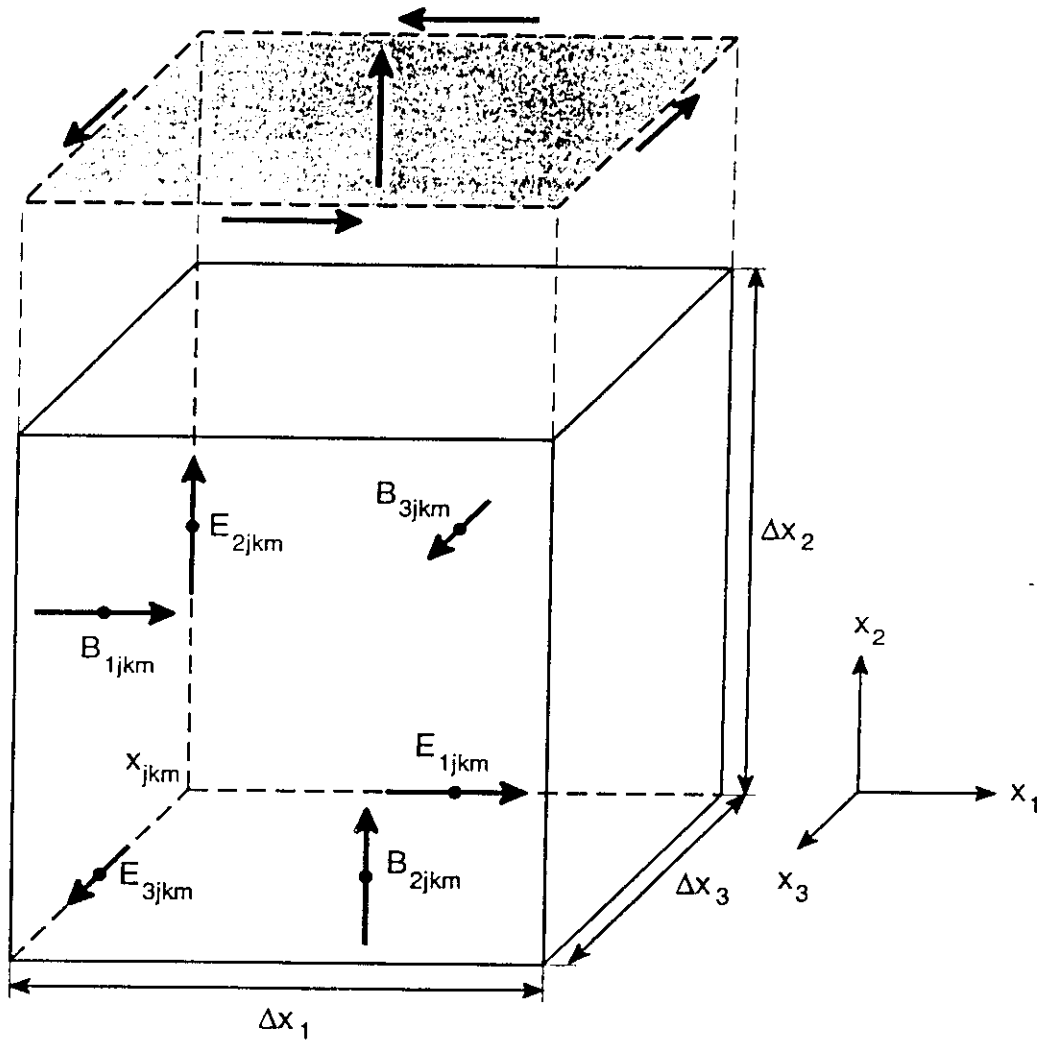

Figure 16: Fields defined on the Yee mesh. Currents, not shown, are co-located with the corresponding electric field components. Exploded view shows an integration surface.

we can write a general finite-difference form relation for advancing all components of the electric flux:

$$\delta_t D_i = \delta_j H_k - \delta_k H_j, \tag{79}$$

where i, j, and k denote the indices of an orthogonal right-handed set of coordinates. The full set of difference equations for Ampere's law is formed by cycling over these indices. In Eq. 79, δ_q denotes some finite-difference operator with respect to the variable q.

Faraday's law can be evaluated in the same fashion, starting from the differential form,

$$\frac{\partial \mathbf{B}}{\partial t} = -\nabla \times \mathbf{E}, \tag{80}$$

to form a general finite difference form of Faraday's law:

$$\delta_t B_i = -\delta_j E_k + \delta_k E_j. \tag{81}$$

The constitutive equations couple Eqs. 79 and 81:

$$\begin{aligned} \mathbf{D} &= \epsilon \mathbf{E}, \text{ and} \\ \mathbf{B} &= \mu \mathbf{H}. \end{aligned} \tag{82}$$

The most common implementation of Eqs. 79 and 81 in PIC codes uses a center difference for δ, and places the fields on the mesh as shown in Fig. 16, called the leapfrog algorithm [2]. That is, D, E and J are defined at the midpoints of the segments connecting mesh nodes, while B and H are defined similarly on a mesh displaced by one half cell in each dimension. The center difference form of Ampere's law on a uniform orthogonal mesh becomes:

$$\frac{D_i^t - D_i^{t-\Delta t}}{\Delta t} = \frac{H_{k,x_j+\Delta x_j/2}^{t-\Delta t/2} - H_{k,x_j-\Delta x_j/2}^{t-\Delta t/2}}{\Delta x_j} - \frac{H_{j,x_k+\Delta x_k/2}^{t-\Delta t/2} - H_{j,x_k-\Delta x_k/2}^{t-\Delta t/2}}{\Delta x_k} - J_i^{t-\Delta t/2}. \tag{83}$$

Here, only subscripts pertaining to the direction of the derivative have been included for compactness. Similarly, the center difference form of Faraday's law on a uniform orthogonal mesh becomes:

$$\frac{B_i^{t+\Delta t/2} - B_i^{t-\Delta t/2}}{\Delta t} = -\frac{E_{k,x_j+\Delta x_j/2}^t - E_{k,x_j-\Delta x_j/2}^t}{\Delta x_j} + \frac{E_{j,x_k+\Delta x_k/2}^t - E_{j,x_k-\Delta x_k/2}^t}{\Delta x_k}. \tag{84}$$

Thus, the curl equations can be advanced in time after closing with the constitutive relations, Eq. 82. These equations are solved consecutively, so that the fields leapfrog forward in time. The leapfrog algorithm is considered explicit in that the field updates only depend upon past field values. This scheme is second order accurate in both time and space for uniform cells.

5.1 Dispersion of Wave Equation

The stability of the center difference for the wave equation describes its accuracy and stability properties. Consider the wave equation in one dimension:

$$\frac{\partial^2 \psi}{\partial t^2} = c^2 \frac{\partial^2 \psi}{\partial x^2} \tag{85}$$

Center differencing,

$$\psi_j^{t+\Delta t} = \left(c\frac{\Delta t}{\Delta x}\right)^2 \left(\psi_{j+1}^t - 2\psi_j^t + \psi_{j-1}^t\right) + 2\psi_j^t - \psi_j^{t-\Delta t}. \tag{86}$$

For sinusoidal waves,

$$\psi(x,t) = \exp\left[i\left(\omega t - kx\right)\right] \tag{87}$$

$$\psi_j^t = \exp\left[i\left(\omega t - \tilde{k} j \Delta x\right)\right] \tag{88}$$

with $\tilde{k}$ the numerical wavenumber.

Combining Eqs. 86 and 88:

$$\exp\left(i\omega\Delta t\right) = \left(c\frac{\Delta t}{\Delta x}\right)^2 \left[\exp\left(-i\tilde{k}\Delta x\right) - 2 + \exp\left(i\tilde{k}\Delta x\right)\right] + 2 - \exp\left(-i\omega\Delta t\right) \tag{89}$$

$$\frac{\exp\left(i\omega\Delta t\right) + \exp\left(-i\omega\Delta t\right)}{2} = \left(c\frac{\Delta t}{\Delta x}\right)^2 \left(\frac{\exp\left(i\tilde{k}\Delta x\right) + \exp\left(-i\tilde{k}\Delta x\right)}{2} - 1\right) + 1 \tag{90}$$

Then the dispersion equation becomes:

$$\cos\left(\omega\Delta t\right) = \left(c\frac{\Delta t}{\Delta x}\right)^2 \left[\cos\left(\tilde{k}\Delta x\right) - 1\right] + 1 \tag{91}$$

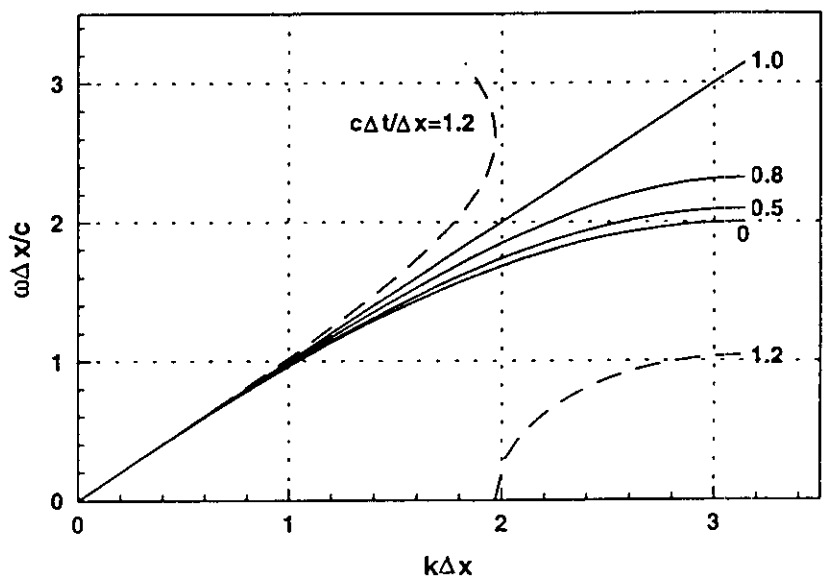

Figure 17: Vacuum dispersion curve for leapfrog difference scheme for wave equation.

For $c\Delta t/\Delta x = 1$, the numerical wavenumber is $\tilde{k} = \pm\omega/c = k$. Similarly, for $\Delta t \to 0$ and $\Delta x \to 0$, $\tilde{k} = \pm\omega/c = k$.

For $c\Delta t/\Delta x > 1$ (the Courant-Levy stability condition), a rapidly growing imaginary root is given by

$$\frac{\omega_i \Delta x}{c} = \frac{\Delta x}{c\Delta t} \cosh^{-1}\left[\left(c\frac{\Delta t}{\Delta x}\right)^2 [\cos(k\Delta x) - 1] + 1\right], \tag{92}$$

which occurs for

$$k\Delta x > \cos^{-1}\left[1 - 2\left(\frac{\Delta x}{c\Delta t}\right)^2\right]. \tag{93}$$

In multiple dimensions the Courant-Levy stability criterion on the time step given by:

$$\Delta t \le \frac{1}{c}\left(\sum_i \frac{1}{(\Delta x_i)^2}\right)^{-1/2}, \tag{94}$$

where the index i sums over the coordinate indices, and Δx_i denotes the grid spacing in the ith coordinate direction.

5.2 Electromagnetic Boundary Conditions

- Conductors: set $E_{\parallel} = 0$ along ideal conductors.
- 1st order Surface Impedance Boundary Condition [2]: (SIBC) Relates tangential field components. In frequency domain the impedance is given by:

$$Z(\omega) = \frac{E_j(\omega)}{H_k(\omega)} = R + i\omega L, \tag{95}$$

where R is the resistance and L is the inductance. A similar relation exists for the other tangential field components. In the time domain,

$$E_j(t) = RH_k(t) + L\frac{\partial}{\partial t}H_k(t). \tag{96}$$

Note that free space is given by $L = 0$, $R = \mu_0 c = 120\pi$ ohms. For a boundary in the j, k plane, the finite difference form becomes

$$E_j^t = RH_{k*}^t + L\frac{H_{k*}^{t+\Delta t/2} - H_{k*}^{t-\Delta t/2}}{\Delta t}, \tag{97}$$

where the * refers to the fact that H must be co-located with the electric field. The magnetic field at the integral timestep is approximated by:

$$H_{k*}^t = \frac{H_{k*}^{t+\Delta t/2} + H_{k*}^{t-\Delta t/2}}{2}. \tag{98}$$

Then Eq. 97 becomes:

$$E_j^t = \left(\frac{R}{2} + \frac{L}{\Delta t}\right)H_{k*}^{t+\Delta t/2} + \left(\frac{R}{2} - \frac{L}{\Delta t}\right)H_{k*}^{t-\Delta t/2} \tag{99}$$

The magnetic field on the boundary is obtained from the Ampere-Maxwell relation:

$$H_{k*}^{t+\Delta t/2} = H_{k,x_j+\Delta x_j/2}^{t+\Delta t/2} + \frac{\Delta x_i}{2}\left(\frac{D_j^{t+\Delta t} - D_j^t}{\Delta t} + J_j^{t+\Delta t/2}\right). \tag{100}$$

This method is first order accurate in Δx.

- 2nd order SIBC: same as the first order, except that the Ampere-Maxwell relation is taken at $\Delta x/4$ in from the edge:

$$H_{k*}^{t+\Delta t/2} = H_{k,x_j+\Delta x_j/2}^{t+\Delta t/2} + \frac{\Delta x_i}{2}\left(\frac{D_{j*}^{t+\Delta t} - D_{j*}^{t}}{\Delta t} + J_{j*}^{t+\Delta t/2}\right), \quad (101)$$

where the j^* terms are evaluated at $\Delta x_i/4$ using second order estimates:

$$J_{j*}^{t+\Delta t/2} = \frac{1}{4}J_{j,\Delta x_i/2}^{t+\Delta t/2} + \frac{3}{4}J_{j,0}^{t+\Delta t/2}, \text{ and} \quad (102)$$

$$D_{j*}^{t+\Delta t} = \frac{1}{4}D_{j,\Delta x_i/2}^{t+\Delta t} + \frac{3}{4}D_{j,0}^{t+\Delta t}. \quad (103)$$

The values of D_{j*}^{t} can be stored from previous timesteps.

- Many other electromagnetic boundary conditions are possible.

6 Coupling Fields to Particles

The particle and field algorithms described above are coupled together through the source terms in Maxwell's equations.

6.1 Electrostatic Coupling

- Nearest Grid Point (NGP) Weighting – fast, simple bc, noisy
- Linear Weighting – relatively fast, simple bc, less noisy
- Higher Order Weighting Schemes – slow, complicated bc, low noise
- Self-Force: asymmetric weighting ("energy conserving scheme") results in self-force

Define

$$\mathbf{w} = \mathbf{x}_i - \mathbf{X}_{jkm}, \quad (104)$$

where $\mathbf{x}_i$ refers to the position of the ith particle, and $\mathbf{X}_{jkm}$ is the position of the nearest lower mesh node.

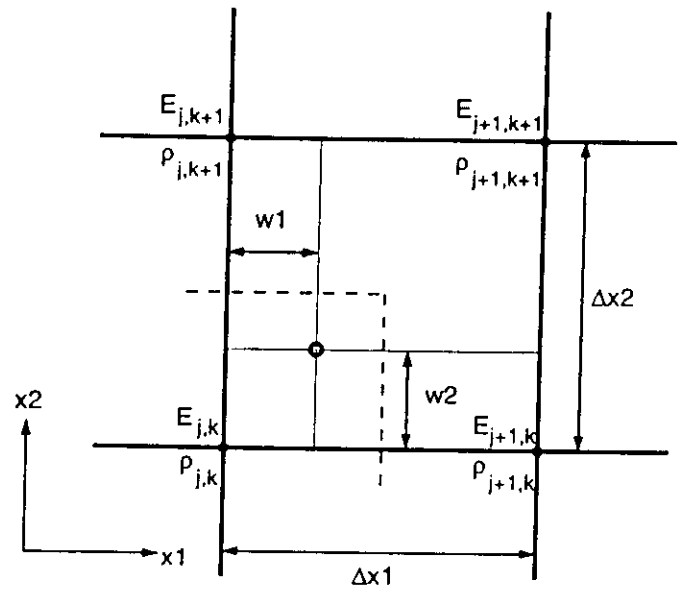

Figure 18: Weighting charge to the grid, and fields to particles.

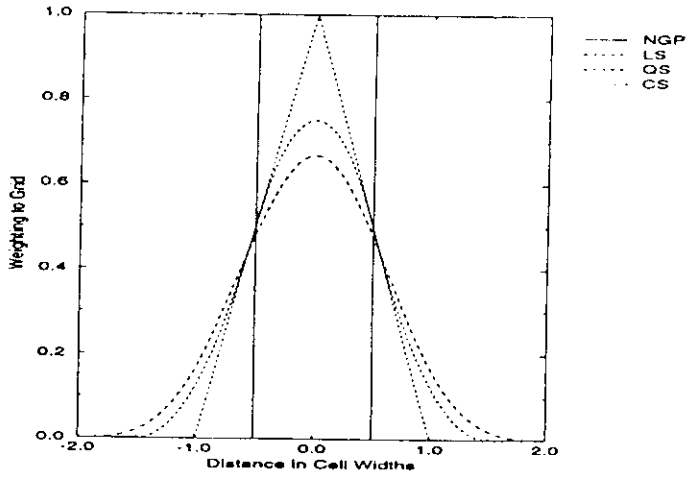

Figure 19: Particle shapes for nearest grid point (NGP), linear spline (LS), quadratic spline (QS), and cubic spline (CS) particle weightings.

Algorithm	τ_{run}	τ_H	τ_H/τ_{run}
NGP-NGP	1.0	1.0	1.0
LS-NGP*	1.26	0.62	0.49
LS-LS	1.63	38.4	23.6
QS-LS*	2.31	10.0	4.33
QS-QS	2.68	168.9	63.0
CS-QS*	3.23	108.3	33.5
CS-CS	3.71	456.6	123.1

Table 1: Performance and heating rates for a number of weightings [15]. Energy conserving schemes are marked with an '*'. Note that the run times here, τ_{run}, were computed in a periodic system; the higher order weightings are more costly in a bounded system.

Then the linear weighting algorithm would result in the charge of a single particle being weighted to the surrounding nodes:

$$Q_{j,k,m} = q_i (1 - w_j)(1 - w_k)(1 - w_m), \tag{105}$$

$$Q_{j+1,k,m} = q_i w_j (1 - w_k)(1 - w_m), \tag{106}$$

$$Q_{j,k+1,m} = q_i (1 - w_j) w_k (1 - w_m), \tag{107}$$

$$Q_{j,k,m+1} = q_i (1 - w_j)(1 - w_k) w_m, \tag{108}$$

$$Q_{j+1,k+1,m} = q_i w_j w_k (1 - w_m), \tag{109}$$

$$Q_{j+1,k,m+1} = q_i w_j (1 - w_k) w_m, \tag{110}$$

$$Q_{j,k+1,m+1} = q_i (1 - w_j) w_k w_m, \tag{111}$$

$$Q_{j+1,k+1,m+1} = q_i w_j w_k w_m. \tag{112}$$

The charge is accumulated in this manner for all particles. The charge density is computed using $\rho_{j,k,m} = Q_{j,k,m}/V_{j,k,m}$, where $V_{j,k,m}$ is the volume of the cell centered on the j,k,mth mesh node.

6.2 Electromagnetic Coupling

- Charge conserving schemes
- Symmetric current weighting (e.g. bilinear)

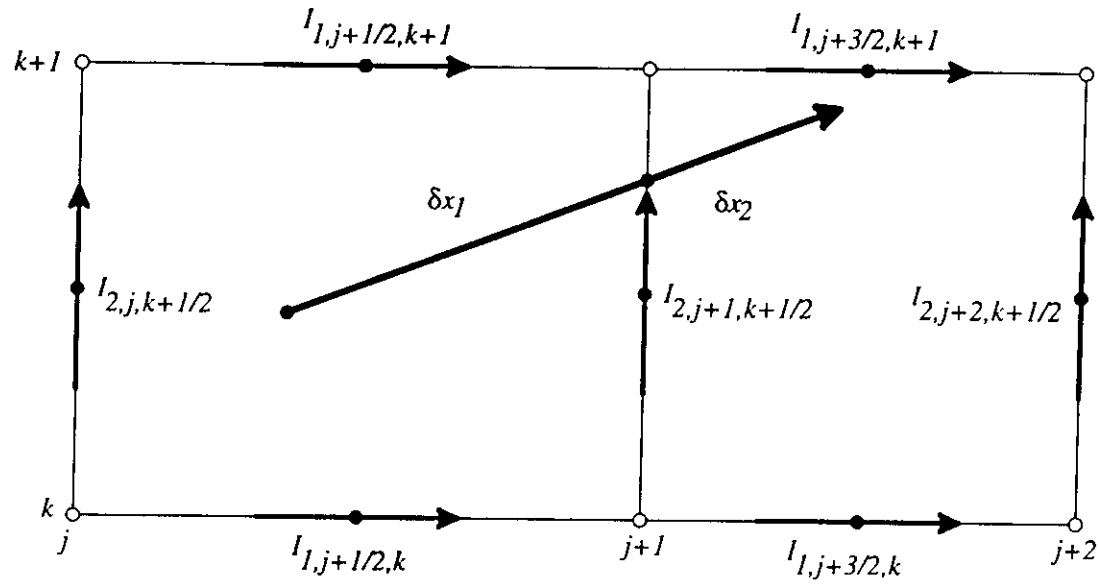

Figure 20: Current elements for a multi-cell particle motion.

Current can be weighted using either a charge conserving method, or an algorithm equivalent to the charge density weighting algorithm. When the latter scheme is employed, charge is not identically conserved on the mesh, so periodic explicit enforcement of Gauss's law is required to reduce buildup of dipoles.

Using the definition of $\mathbf{w}$ given in Eq. 104, and also defining

$$\Delta \mathbf{w} = \mathbf{w}^{t+\Delta t} - \mathbf{w}^t, \text{ and} \tag{113}$$

$$\bar{\mathbf{w}} = \left(\mathbf{w}^{t+\Delta t} + \mathbf{w}^t\right)/2, \tag{114}$$

we can write the two-dimensional charge conserving currents generated in the first cell due to the particle motion shown in Fig. 20:

$$I_{1,x_j+\Delta x_j/2,x_k} = \sum_i \frac{q_i}{\Delta t} \Delta w_1 \left(1 - \bar{w}_2\right), \tag{115}$$

$$I_{1,x_j+\Delta x_j/2,x_k+\Delta x_k} = \sum_i \frac{q_i}{\Delta t} \Delta w_1 \bar{w}_2, \tag{116}$$

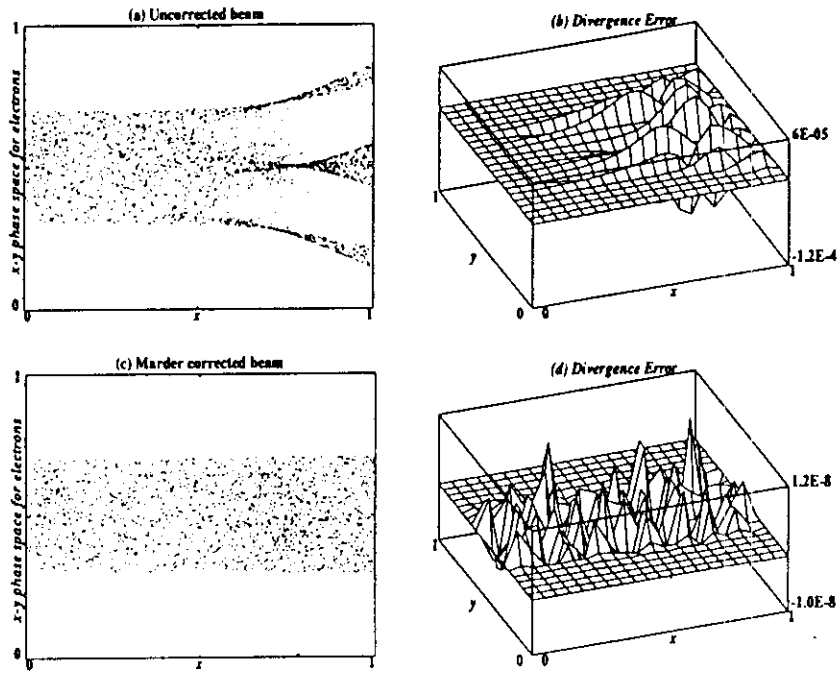

Figure 21: Accumulation of divergence error due to bilinear current weighting (100 beam transit times, about $\omega_p \tau = 50$).

$$I_{2,x_j,x_k+\Delta x_k/2} = \sum_i \frac{q_i}{\Delta t} (1 - \bar{w}_1) \Delta w_2, \tag{117}$$

$$I_{2,x_j+\Delta x_j,x_k+\Delta x_k/2} = \sum_i \frac{q_i}{\Delta t} \bar{w}_1 \Delta w_2. \tag{118}$$

When cell edges are crossed, the above set of equations is applied for each cell traversed, using the segments of movement falling within the respective cell. This method is equivalent to Morse and Nielson [18] for particle motion within a single cell; for multiple cells it is equivalent to the method of Eastwood [8] and Villaseñor and Buneman [35].

A non-charge conserving scheme, such as bilinear weighting, would have the same form as the charge weighting scheme outlines in Eqs. 105-112, with q_i replaced with $q_i \mathbf{v} \cdot \hat{\mathbf{J}}$, where $\hat{\mathbf{J}}$ is the coordinate direction of the relevant current component. Non-charge conserving schemes require a correction to avoid build-up of charge dipoles.

6.2.1 Charge Conservation

Charge conserving current weighting methods weight one order higher in the transverse direction (e.g. NGP along J, linear transverse to J). For the low order (efficient) weightings, this can introduce noise into the system. Higher order (e.g. linear-quadratic) current weighting is expensive, and the boundary conditions are more difficult.

Non-charge conserving methods (e.g. bilinear) can violate the continuity equation [16],

$$\nabla \cdot \mathbf{J} = -\frac{\partial \rho}{\partial t}, \tag{119}$$

in turn causing errors in the irrotational part of **E**.

The **Boris correction** [2]:

$$\mathbf{E}_{cor} = \mathbf{E} - \nabla \delta\Phi \tag{120}$$

$$\nabla \cdot \varepsilon \mathbf{E}_{cor} = \rho \tag{121}$$

where $\mathbf{E}_{cor}$ is the corrected field satisfying Gauss's Law, **E** is the uncorrected field computed from the curl equation, and $\nabla\delta\Phi$ is the correction to apply.

$$\nabla \cdot \varepsilon \left(\mathbf{E} - \nabla \delta\Phi\right) = \rho \tag{122}$$

so $\delta\Phi$ must satisfy

$$\nabla \cdot \varepsilon \nabla \delta\Phi = \nabla \cdot \varepsilon \mathbf{E} - \rho, \tag{123}$$

which can be solved by any number of direct or iterative schemes.

The **Langdon-Marder correction** [13]:

$$\varepsilon \mathbf{E}^t_{cor} = \varepsilon \mathbf{E}^t + \Delta t \nabla \left[d \left(\nabla \cdot \varepsilon \mathbf{E}^t - \rho^t \right) \right] \tag{124}$$

where d is the diffusion parameter, stable for

$$d \leq \frac{1}{2\Delta t} \left(\frac{\Delta x^2 \Delta y^2}{\Delta x^2 + \Delta y^2} \right) \equiv d_{max} \tag{125}$$

Since both corrections are the gradient of a scalar, the corrections are irrotational ($\nabla \times \nabla\delta\Phi \equiv 0$).

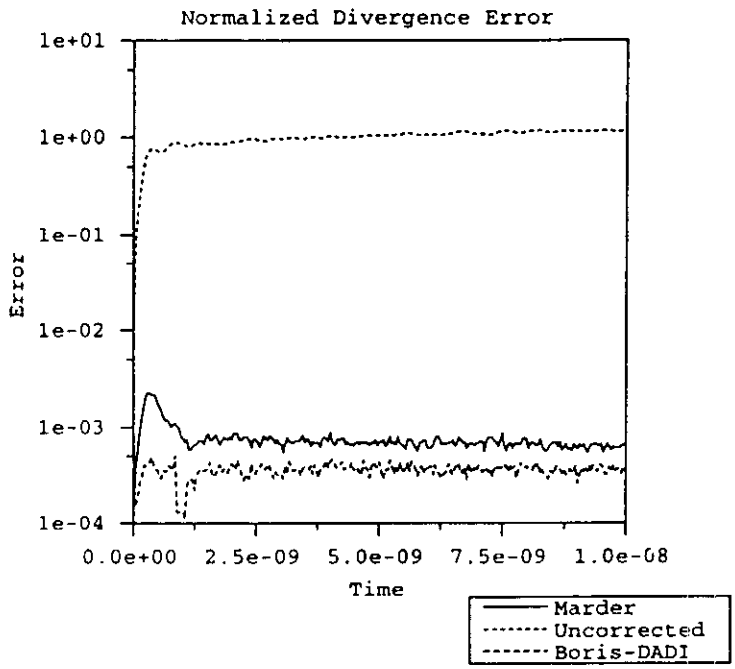

Figure 22: Divergence error in a thermal plasma ($T_e = 4700$ eV, $n_e = n_i = 10^{10}$ cm^{-3}, $M/m = 40000$, $T_i = 1.87$ eV).

7 Plasma Model

The standard particle-in-cell (PIC) model has always included the capability to model ions. Recent work in the simulation of gas discharges has added the ability to include charged-particle interactions with neutral atoms and molecules using a Monte Carlo collision (MCC) model [30]; the enhanced model is often called PIC-MCC. In addition to the Monte Carlo collision model, a number of other advances are described which have made it possible to model the disparate timescales that occur when including ions and background gases, including subcycling of particles and fields, noise filtering, and particle splitting/coalescing.

7.1 Monte Carlo Collision Model

The MCC model statistically describes the collision processes, using cross sections for each reaction of interest. An electrostatic MCC model used for gas discharges [30] is adapted for relativistic electromagnetic simulations. The general scheme for the PIC-MCC is shown in Fig. 1.

Consider a set of particles incident on a second set of targets. For the ith incident particle of energy $\mathcal{E}_i = \frac{1}{2}mv_i^2$, the probability, P_i, of a collision event can be written

$$P_i = 1 - \exp\left[-n_g\left(\mathbf{x}\right)\sigma_T(\mathcal{E}_i)v_i\Delta t\right], \tag{126}$$

where the total cross section is the sum over all processes, $\sigma_T(\mathcal{E}_i) = \sum_j \sigma_j(\mathcal{E}_i)$. Here $n_g(\mathbf{x})$ is the spatially varying target density, v_i is the incident speed, and Δt is the time interval.

For a pure Monte Carlo method [20], the probability is inverted to solve for the time interval between collisions for the ith particle:

$$\Delta t_i = -\frac{\ln\left(1-R\right)}{n_g\left(\mathbf{x}\right)\sigma_T(\mathcal{E}_i)v_i}, \tag{127}$$

where $0 < R < 1$ is a uniformly distributed random number. The equations of motion can then be integrated for Δt_i before applying the collision behavior. While this technique has the benefit of taking the longest possible timestep, resulting in maximum computational efficiency, it is evident that the particles are no longer synchronized in time. This method can only be applied when space charge and self-field effects can be neglected, and may be useful in iterative gun code calculations, for example. Nonetheless, once a collision

event does occur, the resulting dynamics are computed in the same manner as in PIC-MCC.

There is a finite probability that the ith particle will undergo more than one collision in the time interval Δt. For nearly lossless collisions, such as elastic scattering with a massive target, the probability of n collisions in a time interval Δt is P_i^n, so the total number of missed collisions can be written

$$r_i \approx \sum_{k=2}^{\infty} P_i^k = \frac{P_i^2}{1 - P_i}. \tag{128}$$

If $P_i \ll 1$, $r_i \approx P_i^2$ provides a measure of the under-representation of the collision operator. Hence, traditional PIC-MCC codes are constrained by $\nu_{T,\max}\Delta t \ll 1$ for accuracy, where $\nu_{T,\max} = \max[n_g(\mathbf{x})\,\sigma_T(\mathcal{E}_i)v_i]$ is the maximum collision frequency in space and energy. XOOPIC [34] does not suffer from this limitation, modeling multiple collisions per particle per timestep.

Computing the collision probability for each particle each timestep is computationally expensive, since it involves computing the particle energy, a square root to obtain the speed, and either interpolation of tabled cross sections or computation of a curve fit for each process for every particle. The cost of the MCC can exceed significantly the cost of integrating the equations of motion, so we seek a more efficient method.

Defining a maximum collision frequency in space and energy,

$$\nu_{\max} = \max_{\mathbf{x}}\left(n_g(\mathbf{x})\right) \max_{\mathcal{E}}\left(\sigma_T(\mathcal{E})v\right), \tag{129}$$

we can write a total collision probability independent of particle energy and position, $P_T = 1 - \exp\left(-\nu_{\max}\Delta t\right)$. The physical interpretation is shown in Fig. 23. The collision frequencies are incrementally summed for electron impact on neon, with ν_1 representing elastic scattering, ν_2 representing all excitations summed, and ν_3 representing electron impact ionization. The area between $\nu_{\max}$ and $\nu_1 + \nu_2 + \nu_3$ represents the null collision event.

The fraction of particles undergoing a collision each time step is now given by P_T, and the particles can be chosen at random from the particle list. Depending upon the implementation, duplicates may be discarded, resulting in the error described in Eq. 128. A more accurate method is to allow a particle to be chosen multiple times at random, applying each collision sequentially. Once the particles undergoing collisions have been selected, the type of collision for each particle is determined by choosing a random

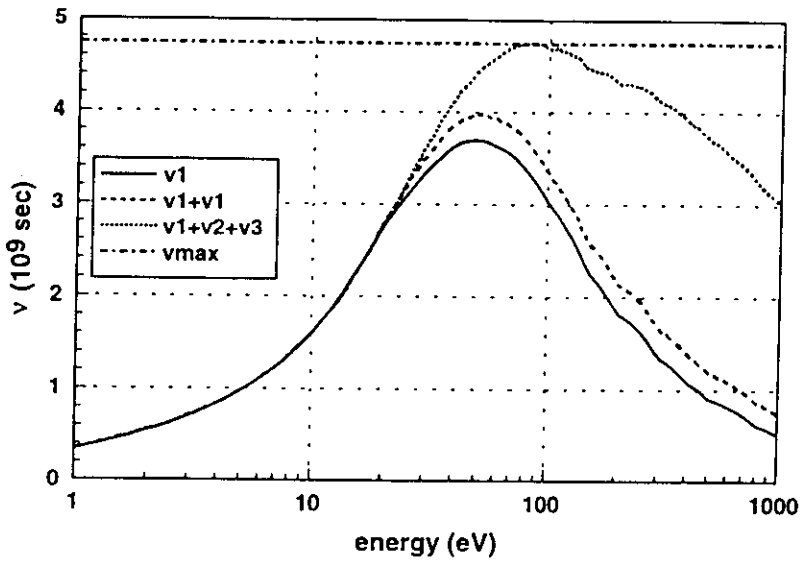

Figure 23: Summed collision frequencies for the null collision method.

number, $0 \leq R \leq \nu_{\max}$. R is mapped onto the collision frequencies shown in Fig. 23. This method is called the null collision method, because an energy dependent null collision frequency has been added in order to form the energy independent probability which eliminates the computation of energies and cross sections for all particles each timestep.

Next, we consider the collision dynamics of electron-neutral collisions. A number of electron-neutral collision events are possible, including elastic scattering ($e + A \rightarrow e + A$), excitation ($e + A \rightarrow e + A^*$), and ionization ($e + A \rightarrow e + A^+ + e$). Here, e represents an electron, A represents a neutral atom, A^* is an excited state of A, and A^+ is the singly ionized state of A.

First, consider electron-neutral elastic collisions. The differential cross section is required to compute the final velocity of the incident electron. For elastic scattering of electrons in argon, one possible cross section is [28]:

$$\frac{\sigma(\mathcal{E}_i, \chi)}{\sigma(\mathcal{E}_i)} = \frac{\mathcal{E}_i}{4\pi \left[1 + \mathcal{E}_i \sin^2(\chi/2)\right] \ln(1 + \mathcal{E}_i)}, \tag{130}$$

with incident electron energy $\mathcal{E}_i$ in eV,and χ is the scattering angle. It should be noted that many other choices are possible; for example, see [11] for differential ionization cross sections in a number of gases. The cumulative

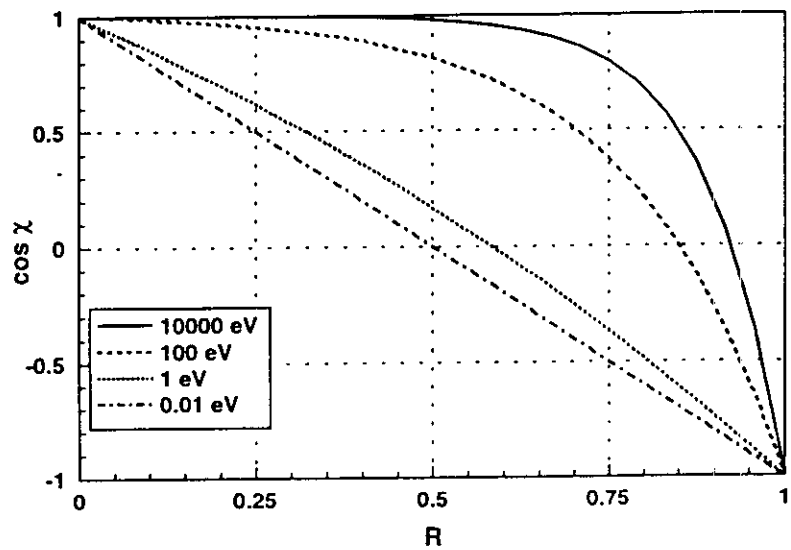

Figure 24: Scattering angle distribution for a range of energies.

distribution function is:

$$R = \frac{\int_0 \chi \sigma(\mathcal{E}, \chi) \sin \chi d\chi}{\int_0 \pi \sigma(\mathcal{E}, \chi) \sin \chi d\chi}. \tag{131}$$

If R is a uniformly distributed random number $0 \leq R \leq 1$, the scattering angle becomes:

$$\cos \chi = \frac{2 + \mathcal{E}_i - 2\left(1 + \mathcal{E}_i\right)^R}{\mathcal{E}_i}. \tag{132}$$

The scattering angles for electrons incident on argon are shown in Fig. 24. The angular distribution varies from isotropic at 10 mV to small-angle dominated at 10 kV. The azimuthal angle is uniformly distributed, $0 \leq \theta \leq 2\pi$.

Once the scattering angle is specified, the fractional energy loss in the scattering event can be computed by classical collision mechanics [17]:

$$\Delta\mathcal{E} = \frac{2m}{M}(1 - \cos \chi)\mathcal{E}_i. \tag{133}$$

Next, we consider electron-neutral inelastic collisions, such as excitation and ionization. For ionization, the energy balance is $\mathcal{E}_f = \mathcal{E}_i - \mathcal{E}_2 + \mathcal{E}_N -$

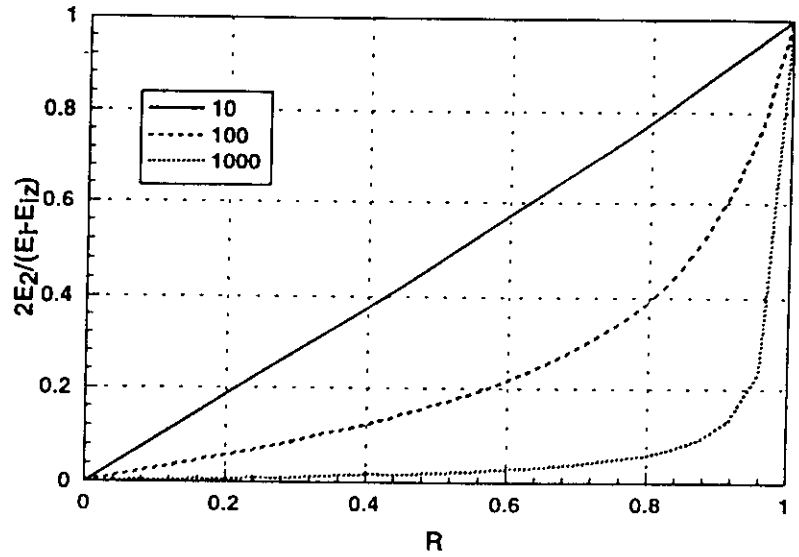

Figure 25: Normalized scattered electron energy distribution for $10 \leq \mathcal{E}_i \leq 1000$ eV.

$\mathcal{E}_+ - \mathcal{E}_{iz}$,where $\mathcal{E}_i$ and $\mathcal{E}_f$ are the initial and final primary electron energies, $\mathcal{E}_2$ is the energy of the ionization electron, $\mathcal{E}_N$ is the neutral energy, $\mathcal{E}_+$ is the ion energy, and $\mathcal{E}_{iz}$ is the ionization threshold. Since the mass of the electron is small compared to the mass of the neutral, $m \ll M$, we neglect the momentum change of the neutral, so that $\mathcal{E}_N = \mathcal{E}_+$. For excitation, the energy balance becomes $\mathcal{E}_f = \mathcal{E}_i - \mathcal{E}_{ex}$, where $\mathcal{E}_{ex}$ is the excitation threshold.

For ionization at low $\mathcal{E}_i$, a differential cross section may be chosen of the form [19]

$$S(\mathcal{E}_i, \mathcal{E}_2) = \frac{\sigma_{iz}(\mathcal{E}_i) B(\mathcal{E}_i)}{\arctan\left\{[\mathcal{E}_i - \mathcal{E}_{iz}]/[2B(\mathcal{E}_i)]\right\} [\mathcal{E}_2^2 + B^2(\mathcal{E}_i)]}. \tag{134}$$

Here, $B(\mathcal{E}_i)$ is a known function for many gases. Similar differential ionization cross sections for a series of gases are given in [11]. Inverting the distribution,

$$R = \frac{\int_0^{\mathcal{E}_2} S(\mathcal{E}_i, \mathcal{E}_2') d\mathcal{E}_2'}{\int_0^{(\mathcal{E}_i - \mathcal{E}_{iz})/2} S(\mathcal{E}_i, \mathcal{E}_2') d\mathcal{E}_2'} \tag{135}$$

gives the energy of the ionization electron:

$$\mathcal{E}_2 = B(\mathcal{E}_i) \tan\left[R \arctan\left(\frac{\mathcal{E}_i - \mathcal{E}_{iz}}{2B(\mathcal{E}_i)}\right)\right]. \tag{136}$$

Although the primary and ionization electrons are indistinguishable, we have chosen the convention that the more energetic electron is the primary. In Fig. 25, the energy of the ionization electron normalized to the maximum energy, $\mathcal{E}_{2,\max} = \frac{1}{2}(\mathcal{E}_i - \mathcal{E}_{iz})$, is plotted for a number of incident electron energies. The energy is distributed uniformly at low energies, and the normalized ionization electron energy is reduced significantly at higher energies.

In the high-energy regime, the first Born approximation predicts the differential cross section [25]:

$$f^{(1)}(\chi) = -\frac{2m}{\hbar^2} \frac{1}{2k_i \sin(\chi/2)} \int_0^\infty rV(r) \sin(2k_i \sin(\chi/2))\, dr \tag{137}$$

where k_i is the incident electron wavenumber, $V(r)$ is the interaction potential. Using a potential appropriate to the collision of interest, one can obtain the energy and angular distributions as discussed above. For the Coulomb potential, $V(r) = Z_1 Z_2 e^2/r$, the differential cross section becomes the classical Rutherford scattering cross section:

$$\frac{d\sigma}{d\Omega} = \frac{1}{16}\left(\frac{Z_1 Z_2 e^2}{\mathcal{E}_i}\right)^2 \frac{1}{\sin^4(\chi/2)}. \tag{138}$$

Ion-neutral collisions are similar to electron-neutral collisions, except the collision mechanics must be performed in the rest frame of the neutral since the momenta are similar, $v_i \sim v_N$. Examples of ion-neutral collisions include elastic scattering ($A^+ + A \rightarrow A^+ + A$), and charge exchange ($A^+ + A \rightarrow A + A^+$). Here, A represents the neutral atom and A^+ represents the singly ionized state of A. Many other reactions are possible, but are not addressed here.

First, the velocity of the ion is converted to the rest frame of the neutral using $\mathbf{v}_i' = \mathbf{v}_i - \mathbf{v}_N$. The ion energy is then computed using $\mathcal{E}_i = M_i \mathbf{v}_i' \cdot \mathbf{v}_i'/2$. For elastic scattering, the scattered ion energy can be written:

$$\mathcal{E}_f = \left(1 - \frac{2M_i M_N}{(M_i + M_N)^2}(1 - \cos\Theta)\right)\mathcal{E}_i \tag{139}$$

where $\cos\chi = \sqrt{1-R}$ for isotropic scattering, and Θ is the scattering angle in the center of mass frame. The subscripts i and N refer to the incident ion and neutral respectively. For $M_i = M_N$, $\Theta = 2\chi$, where χ is the scattering angle in the laboratory frame, and the scattered ion energy becomes $\mathcal{E}_f = \mathcal{E}_i \cos^2\chi$. The azimuthal angle is chosen randomly, and the scattered velocity in the rest frame of the neutral is constructed using the angle Θ and the random azimuthal angle in conjunction with the magnitude satisfying $\mathcal{E}_f = M_i \mathbf{v}_f' \cdot \mathbf{v}_f'/2$. The resulting velocity is then converted back to the laboratory frame using $\mathbf{v}_f = \mathbf{v}_f' + \mathbf{v}_N$.

Charge exchange uses the same process for computing the probability, but the neutral velocity is chosen from a prescribed analytic distribution. The neutral identity is then exchanged with the ion.

7.2 Subcycling

The wide variation of timescales requires use of a number of techniques to accelerate the computation. The cost can be reduced to that of fastest species (electrons) by subcycling the slower species; that is, advancing the slower species less frequently than the faster species and the fields using proportionally larger timesteps. The maximum subcycling ratio is given by:

$$\frac{\Delta t_i}{\Delta t_e} = \frac{\omega_{pe}}{\omega_{pi}} = \sqrt{\frac{M}{m}}. \tag{140}$$

The efficiency becomes $\eta = (N_e + N_i \Delta t_e/\Delta t_i)^{-1}$, where N_e and N_i are the number of electrons and ions, respectively, and Δt_e and Δt_i are the electron and ion timesteps, respectively. For $N_e = N_i$, $50\% \leq \eta \leq 99.6\%$ for argon. A narrow band instability occurs for $\omega_{pe}\Delta t_i \approx l\pi$, so it is important in discharge-type problems avoid the instability in the areas where particles are trapped [1][5].

The fields can be advanced on the electron timescale, Δt_e, or they can be subcycled on a faster timescale, Δt_f. Subcycling of particles and fields is shown schematically in Fig. 26.

8 Noise Attenuation Schemes

PIC simulations are generally reasonably low in noise for low density plasmas. However, the noise scales unfavorably with the number of particles,

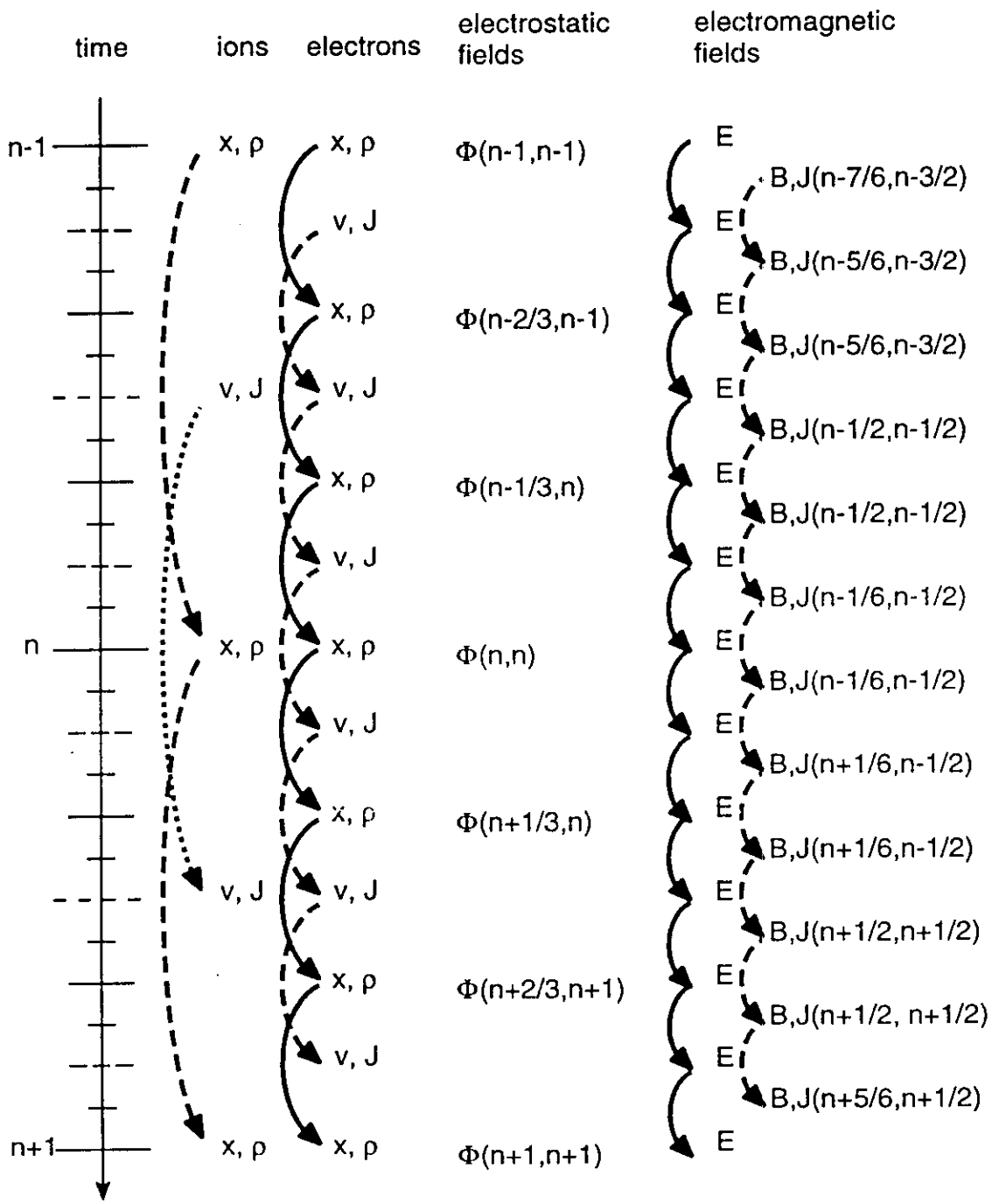

Figure 26: Schematic diagram of particle and field subcycling for electrostatic and electromagnetic codes.

proportionally with $\sqrt{N}$, where N is the number of computer particles. If it is desired to reduce the noise level, either to observe smaller amplitude signals or to reduce the numerical heating [2], a number of noise attenuation techniques exist.

8.1 Fourier Space Filter

Fourier space filtering for PIC codes is described in detail in Birdsall and Langdon [2]. Generally, the method involves attenuating or boosting various wavelength components in Fourier space by operating on the charge density:

$$\rho'(k) = \rho(k) S^2(k), \tag{141}$$

where $S(k)$ is the smoothing function. One method proposed by [2] is:

$$S(k) = \exp\left(a_1 \sin^2(k\Delta x/2) - a_2 \tan^4(k\Delta x/2)\right). \tag{142}$$

Here, $a_1 > 0$ compensates for the errors in the dispersion relation for $k\Delta x \lesssim 1$, and $a_2 > 0$ provides smoothing of short wavelengths.

8.2 Electrostatic Digital Smoothing

This smoothing method applies a digital filter to the charge density distribution. A common digital filter is the binomial or 1-2-1 filter, expressed in one dimension as:

$$\rho_j' = \frac{\rho_{j-1} + 2\rho_j + \rho_{j+1}}{4}. \tag{143}$$

The filter may be applied in multiple passes; each pass produces $\cos^2(k\Delta x)$ filtering. As the number of passes approaches infinity, the binomial filter approaches a Gaussian filter. More generally,

$$\rho_j' = \frac{W\rho_{j-1} + \rho_j + W\rho_{j+1}}{1 + 2W}, \tag{144}$$

where $W = 0.5$ is the binomial filter. Schemes with $W < 0$ produce a compensating filter; $W = -1/6$ produces a compensation that cancels the attenuation of $O\left[(k\Delta x)^2\right]$ of the binomial filter. Efficient techniques to apply the filters in place without duplicate storage are described in [2].

8.3 Electromagnetic Damping Scheme

A technique for temporal filtering of the electromagnetic fields can reduce the noise [22]:

$$\bar{\mathbf{E}}^{n-1} = (1-\zeta)\,\mathbf{E}^{n} + \zeta \bar{\mathbf{E}}^{n-2},\ 0 \le \zeta \le 1/2 \tag{145}$$

$$\mathbf{E}^{n+1} = \mathbf{E}^{n} + c\Delta t \nabla \times \mathbf{B}^{n+1/2} - \epsilon \Delta t \mathbf{J}^{n+1/2} \tag{146}$$

$$\begin{aligned} \mathbf{B}^{n+3/2} &= \mathbf{B}^{n+1/2} - c\Delta t \nabla \times & (147)\\ &\quad \left[(1+\zeta/2)\,\mathbf{E}^{n+1} - \mathbf{E}^{n}/2 + (1-\zeta)\,\bar{\mathbf{E}}^{n-1}/2\right]. & (148) \end{aligned}$$

Here $\bar{\mathbf{E}}$ defines a lag-averaged electric field, and ζ is the damping parameter. This method allows a reduction of the number of particles per Debye sphere, $N_{D,0}/N_{D,f} \sim 10$, for equivalent numerical heating.

9 Numerical Parameters

PIC codes are primarily concerned with the physical parameters of the model. However, some numerical parameters must be considered. These include the grid spacing, Δx, the timestep, Δt and the number of physical particles per computer particle or particle weight, W_p. Although each method is slightly different, and a number of techniques

A common sequence for selecting the numerical parameters is as follows.

- Choose Δx to resolve the smallest important physical feature (e.g. λ_D, λ_{rf}, r_L, boundary feature, etc.)
- If electromagnetic, require:

$$\Delta t \le \frac{1}{c}\left(\sum_i \frac{1}{(\Delta x_i)^2}\right)^{-1/2}, \tag{149}$$

- Require $\Delta t < \Delta x/v_{\max}$ for all species ("particle Courant") for accurate sampling of fields.
- Require $\Delta t < 0.2/\omega_p$ for accuracy when space charge forces are important.

- Require $\Delta t \ll 1/\nu$ when collisions are important in the standard MCC model (modified models like XOOPIC relax this constraint to $\Delta t \lesssim 1/\nu$).
- Require $W_p < \bar{n}\Delta x\alpha/N_p$, where $\bar{n}$ is a typical density, α is the dimensionality of the problem, and N_p is the desired number of particles per cell corresponding to the noise level and numerical heating. For typical simulations, $10 \lesssim N_p \lesssim 100$, where the higher range corresponds to simulations where particles remain trapped for long times.
- Run time becomes: $\tau_{\rm run} \approx (\bar{n}L\alpha/W_p \times T_p + L\alpha/\Delta x\alpha \times T_c) \times t_{\rm final}/\Delta t$, where L is the system length, T_p and T_c are the computer time per particle and cell respectively, and $t_{\rm final}$ is the end-time for the simulation.

10 PTSG Codes

10.1 XPDP1 4.0

10.1.1 Features

- 1 spatial dimension (3 velocities), Cartesian (PDC1=cylindrical, PDS1=spherical)
- uniform mesh
- electrostatic
- RLC, short, open and current driven external circuits
- homogeneous magnetic field at arbitrary angle
- particle subcycling
- spatial filtering of charge density
- Monte Carlo collision package (He, Ar, O, Ne, Xe, etc.)
- emission (drifted Maxwellian flux) and absorption
- initial drifting Maxwellian plasma
- Currently runs on DEC Alpha, Pentium (Pro) Linux, Sun OS, Solaris, HP/UX, IBM RS6000

10.1.2 Demonstrations

- numerical instability
- virtual cathode
- crossed field diode
- dc discharge
- rf discharge

10.2 XOOPIC 2.51

10.2.1 Features

Physics Features

- 2 dimensions ($\partial/\partial_3 \rightarrow 0$), $r - z$ and $x - y$
- Orthogonal, non-uniform mesh
- Electrostatic or full electromagnetic fields
- High frequency EM filtering scheme
- Arbitrary static magnetic fields (eqn. or file)
- Boltzmann and/or inertial electrons
- Fully relativistic particles
- Monte Carlo collision (MCC) package, multiple simple gases (He, Ne, Ar, Xe)
- Arbitrary subcycling of fields and particles
- Arbitrary volumetric plasma sources
- Particle emitters and absorbers
- Secondary electrons from any surface
- Bilinear charge weighting

- Bilinear or charge-conserving current weighting
- Poisson and Langdon-Marder current corrections
- Flexible bc, MKS units or grid units
- Configurable particle and field diagnostics (grid and boundary)
- Orthogonal and stepwise oblique bc
- Flexible diagnostics setup from input file (histories, averaging, striding)
- Input file reads equations (evaluator)
- Magnetic field, time-dependent bc, initial cond., plasma source via evaluator
- User-definable input file variables
- Currently runs on DEC Alpha, Pentium (I, Pro, II) Linux, Sun OS, Solaris, HP/UX, IBM RS6000, MPI-based parallel computers

Boundary Conditions (electrostatic)

- Equipotential surface
- Dielectric
- Currently ideal voltage source circuit

Boundary Conditions (electromagnetic)

- Time-dependent beam emitter (constant or radial particle weights)
- Time-dependent field emitter
- Ideal conductor
- Dielectric
- Gap with time-dependent driving voltage
- Wave launchers (TEM, TE, TM)

- Wave absorbers (TEM, TE, TM)
- Current loops

Contact Information

- Code and manuals available via the internet
  `http://ptsg.eecs.Berkeley.EDU`
- Custom support, maintenance and installation available from Research Institute for Science and Engineering: `rise@langmuir.eecs.Berkeley.EDU`

10.2.2 Demonstrations

- charging dielectric ring
- dc discharge
- electron gun
- beam focused in background gas
- cavity and waveguide modes
- Cerenkov maser
- klystron

References

[1] J. C. Adam, A. Gourdin-Serveniere, and A. B. Langdon. Electron sub-cycling in particle simulation of plasma. *Journal of Computational Physics*, 47:229–244, 1982.

[2] C. K. Birdsall and A. B. Langdon. *Plasma Physics via Computer Simulation.* McGraw-Hill, New York N.Y., 1985.

[3] J. P. Boris. Relativistic plasma simulation - optimization of a hybrid code. In *Proc. Fourth Conf. Numerical Simulation of Plasmas*, pages 3–67, Wash. D.C., 1970.

[4] O. Buneman. Dissipation of currents in ionized media. *Physics Review*, 115:503–517, 1959.

[5] B. I. Cohen. Orbit Averaging and Subcycling in Particle Simulation of Plasmas. In J. U. Brackbill and B. I. Cohen, editors, *Multiple Timescales*, pages 311–333. Academic Press, 1985.

[6] J. M. Dawson. One-dimensional plasma model. *Physics of Fluids*, 5:445–459, 1962.

[7] S. Dushman. *Review of Modern Physics*, 2:381, 1930.

[8] J. W. Eastwood. The virtual particle electromagnetic particle-mesh method. *Computer Physics Communications*, 64:252–266, 1991.

[9] R. H. Fowler and I. W. Nordheim. Electron Emission in Intense Electric Fields. *Proceedings of the Royal Society*, A119:173, 1928.

[10] V. P. Gopinath and B. Vanderberg. Reduction of crossed-field diode transmitted current due to anode secondary emission. *Physics of Plasmas*, 5, 1998.

[11] A. E. S. Green and T. Sawada. *Journal of Atmospheric and Terrestrial Physics*, 34:1719, 1972.

[12] R. W. Hockney and J. W. Eastwood. *Computer Simulation Using Particles*. McGraw-Hill, New York, N.Y., 1981.

[13] A. B. Langdon. On enforcing Gauss's law in electromagnetic particle-in-cell codes. *Computer Physics Communications*, 70:447–450, 1992.

[14] W. S. Lawson. Particle simulation of bounded 1d plasma systems. *J. Comp. Phys.*, pages 253–276, 1989.

[15] P. J. Mardahl and K. L. Cartwright. Reducing numerical heating in 1-d PIC simulations. In C. K. Birdsall, editor, *Annual Progress Report for 1993, Plasma Theory and Simulation Group*. University of California Technical Memorandum, Electronics Research Laboratory, Berkeley, CA 94720, 1993.

[16] P. J. Mardahl and J. P. Verboncoeur. Charge conservation in electromagnetic PIC codes; spectral comparison of Boris/DADI and Langdon-Marder methods. *Computer Physics Communications*, 106:219–229, 1997.

[17] E. W. McDaniel. *Atomic Collisions.* Wiley and Sons, New York, N.Y., 1989.

[18] R. L. Morse and C. W. Nielson. Numerical simulation of the Weibel instability in one and two dimensions. *Physics of Fluids*, 14:830–840, 1971.

[19] C. B. Opal, W. K. Peterson, and E. C. Beaty. *Journal of Chemistry and Physics*, 55:4100, 1971.

[20] B. M. Penetrante and J. N. Bardsley. *Journal of Applied Physics*, 54:6150, 1983.

[21] W. H. Press, B. P. Flannery, S. A. Teukolsky, and W. Y. Vetterling. *Numerical Recipes in C: The Art of Scientific Programming.* Cambridge University Press, Cambridge, UK, 1988.

[22] P. Rambo, J. Ambrosiano, A. Friedman, and D. E. Nielson. Temporal and spatial filtering remedies for dispersion in electromagnetic particle codes. *Proceedings 13th Conf. Numerical Simulation of Plasmas*, 1989.

[23] S. Riyopoulus. *Physics of Plasmas*, 3:1481, 1997.

[24] S. Riyopoulus, D. Chernin, and D. Dialetis. *IEEE Transactions*, ED-44:489, 1997.

[25] J. J. Sakurai. *Modern Quantum Mechanics.* Addison-Wesley, New York, N.Y., 1985.

[26] A. Shih and C. Hor. Secondary emission properties as a function of the electron incidence angle. *IEEE Transactions*, ED-40:824–829, 1993.

[27] K. R. Spangenberg. *Vacuum Tubes.* McGraw-Hill, New York, N.Y., 1948.

[28] M. Surendra, D. B. Graves, and I. J. Morey. Electron heating in low-pressure rf glow discharges. *Applied Physics Letters*, 56:1022–1024, 1990.

[29] V. Vahedi and G. DiPeso. Simultaneous potential and circuit solution for two-dimensional bounded plasma simulation codes. *J. Comp. Phys.*, 131:149–163, 1997.

[30] V. Vahedi and M. Surendra. Monte Carlo collision model for particle-in-cell method: Application to argon and oxygen discharges. *Comp. Phys. Comm.*, 87:179–198, 1995.

[31] J. R. M. Vaughan. A new formula for secondary emission yield. *IEEE Transactions*, ED-36:1963–1967, 1989.

[32] J. R. M. Vaughan. Secondary emission formulas. *IEEE Transactions*, ED-40:830, 1993.

[33] J. P. Verboncoeur, M. V. Alves, V. Vahedi, and C. K. Birdsall. Simultaneous potential and circuit solution for 1d bounded plasma particle simulation codes. *J. Comp. Phys.*, 104:321–328, 1993.

[34] J. P. Verboncoeur, A. B. Langdon, and N. T. Gladd. An object-oriented electromagnetic PIC code. *Comp. Phys. Comm.*, 87:199–211, 1995.

[35] J. Villasenor and O. Buneman. Rigorous charge conservation for local electromagnetic field solvers. *Computer Physics Communications*, 69:306–316, 1992.